

Nanostructuring and Antioxidant Activity of Nanotherapeutics Designed by Self-Assembly of Natural Lipids and Phytochemicals

Thelma Akanchise, Borislav Angelov, Yuru Deng, Takehiko Fujino, Thomas Bizien, and Angelina Angelova*



Cite This: <https://doi.org/10.1021/acsbiomaterials.5c00006>



Read Online

ACCESS |



Metrics & More



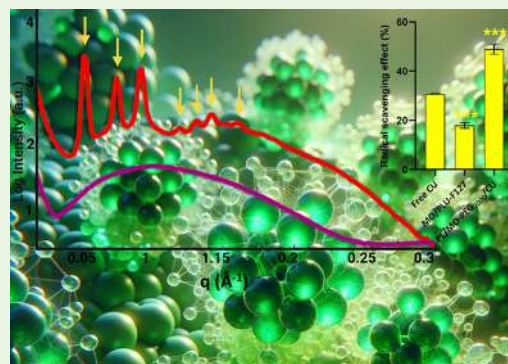
Article Recommendations



Supporting Information

ABSTRACT: Lyotropic liquid crystalline nanostructures formed by self-assembly in an aqueous medium are of fundamental interest and crucial for therapeutic applications, encapsulation of nutraceuticals, tissue engineering, and diagnostics. The biomimetic lipid bilayer building blocks impart biodegradable properties and low toxicity of the created nanoassemblies. The question of synergistic or quenching effects on the resulting bioactivity arises from the coencapsulation of multiple antioxidants (e.g., vitamin E (VitE), curcumin (CU), or coenzyme Q₁₀) in nanocarriers of mixed nonlamellar-phase lipids (e.g., amphiphilic monoglycerides or plasmalogens with long polyunsaturated fatty acid (PUFA) chains). The response to this question should favor phytochemical-based therapies against oxidative stress and inflammatory disorders using sustainable nanomedicines. Herein, we investigate the nanodispersion of multicomponent antioxidant/lipid mixtures using the copolymer Pluronic F127 and three PEGylated amphiphiles (TPGS-PEG₁₀₀₀, MO-PEG₂₀₀₀, and DSPE-PEG₂₀₀₀). The purpose is to establish possible relationships between the amphiphilic pharmaceutical compositions, structural stability, degradability in the biological cell culture medium, and the effects on antioxidant activity. The structures and the topologies of the phytochemical-loaded mesophases were revealed by synchrotron small-angle X-ray scattering and cryogenic transmission electron microscopy imaging. We found that encapsulated antioxidants (CU, Q₁₀, or VitE) fine-tune the lipid bilayer properties and the nanostructure of the self-assembled systems to form lamellar (L), inverted hexagonal (H_{II}), or cubic (Im3m) liquid crystalline phases. The results demonstrated that the composition of the nanoassemblies (lipids, dispersing agents, and antioxidants) governs the structural organization through changes in the interfacial curvature and miscibility effects. A minimal toxicity of the nanoassemblies was observed *in vitro* using the human neuroblastoma cell line (SH-SY5Y). The biodegradability/stability of the nanodispersions was linked with gradual dynamic changes in nanoparticle size distribution in the biological cell culture medium (DMEM). The established enhanced reactive oxygen species (ROS)-scavenging activity of the liquid crystalline nanoformulations is of interest for developing safe pharmaceutical nanosystems for multitargeted delivery of poorly soluble phytochemicals.

KEYWORDS: self-assembled biomaterials, phytochemical antioxidants, lyotropic liquid crystalline mesophases, biodegradable nanoparticles, small-angle X-ray scattering



INTRODUCTION

Engineering of eco-friendly lipid-based nanosystems by self-assembly has gained extensive interest as a reliable, sustainable, and eco-friendly approach for synthesizing nano- and biomaterials.¹ Nanomedicine has rapidly and broadly impacted disease diagnosis, treatment, and prevention. Despite being only a few decades old, research in nanomedicine has already led to the development of a wide range of healthcare products, including the recent COVID-19 vaccines marketed by Pfizer-BioNTech (BNT162b2, Comirnaty) and Moderna (mRNA-1273, Spikevax).^{2,3} The attractiveness of lipid nanoparticles (LNPs) relies on the capability of loading various therapeutic and diagnostic agents, protecting them from degradation, enhancing absorption and improving intracellular penetration,

minimizing systemic toxicity, modifying pharmacokinetics, and overcoming systemic barriers.⁴

Lyotropic lipid liquid crystalline nanoparticles (LCNPs) comprise a promising class of nanomaterials for drug delivery, sustainable nanomedicine, and bioimaging applications. They are classified into lamellar and nonlamellar assemblies based on their supramolecular architectures.^{5–8} The formation of differ-

Received: January 2, 2025

Revised: April 2, 2025

Accepted: May 13, 2025



ACS Publications

© XXXX The Authors. Published by
American Chemical Society

A

<https://doi.org/10.1021/acsbiomaterials.5c00006>
ACS Biomater. Sci. Eng. XXXX, XXX, XXX–XXX

ent nanostructured materials by self-assembly of lyotropic lipids depends on the specific amphiphile geometry and external conditions (pH, salt, temperature, ...).^{8,9} Vesicles and liposomes are currently the most widely used nanocarriers in research and pharmaceutical applications. On the other hand, nonlamellar structures, including cubosomes and hexosomes with their unique nanoarchitectures, are among the most investigated nanosystems as the next-generation nanocarriers.^{10,11} LCNPs have diverse internal structural features, making them versatile nanoself-assemblies that can efficiently encapsulate various bioactive compounds (including small molecule drugs, peptides, proteins, and nucleic acids).^{7,12} The lamellar bilayer phases (L) and the inverted hexagonal structures (H_{II}) represent one- and two-dimensional (1D and 2D) ordered phases. Three-dimensionally (3D) organized hydrated lipid nanostructures can be formed with varying negative curvatures and degree of order, represented by the bicontinuous cubic phase structures [e.g., primitive (P; $Im3m$), diamond (D; $Pn3m$), and gyroid (G; $Ia3d$)] and some micellar cubic phases (e.g., $Fd3m$; I_2). In other cases, an intermediate nonperiodic mesophase called the “melted” cubic or a sponge phase (L_3) forms at interfacial curvatures between those of the lamellar and cubic phases. It features interconnected water channels without periodic organization and greater fluidity than the bicontinuous cubic lipid phases.^{7,13}

The molecular building blocks of LCNPs may include naturally occurring phospholipids or amphiphiles such as monoolein (MO), phytantriol, and long-chain polyunsaturated fatty acids (PUFA), making them biocompatible and biodegradable. Other advantages of LCNPs are their amphiphilic nature and high surface area, which renders them suitable self-assembled eco-friendly objects for high loading of hydrophilic and lipophilic agents.¹⁴ Lipid bilayers protect incorporated drugs against enzymatic degradation. A recent study has shown that cubosomes interact with cells via the fusion of the internal lipid bilayer with the cellular plasma membrane, which may enhance protein function and reduce the degradation of the drug payload within the lysosomes.^{7,15}

The formation of LCNPs is based on a spontaneous self-assembly mechanism that minimizes energy consumption, thus reducing environmental pollution. This simple process is advantageous with regard to the fabrication of various polymer-based nanoparticles and dendrimers where complex formulation routes are often required, or to metallic nanoparticles where surface modification and conjugation of different molecules are needed to achieve biocompatibility and stability.^{1,16} The self-assembly fabrication approach positively impacts the sustainability of the manufacturing process by improving cost-effectiveness and utilizing greener, eco-friendly components, which can favor transitioning from lab-scale to industrial-scale production.

In the present study, three antioxidants, vitamin E (VitE), curcumin (CU), and coenzyme Q_{10} (Q_{10}) are encapsulated in lipid nanocarriers. The purpose is to create and compare various liquid crystalline nanoarrangements loaded with antioxidants (e.g., vesicular, hexagonal, cubosomal, or mixed structures). *In vitro*, the lamellar and nonlamellar nanocarriers are examined for their antioxidant activities against reactive oxygen species (ROS), stability in biological cell culture medium (DMEM), and toxicity profiles. The research hypothesis on the antioxidant activity of LCNPs for drug delivery applications is the following. The encapsulation of plant-based phytochemicals, such as VitE, CU, and Q_{10} , is a “green” way to promote the safe and

environmentally friendly engineering of nanoparticles by self-assembly. VitE and CU are abundant natural substances with antioxidant, antitumor, and anti-inflammatory activities.^{17,18} It has been reported that CU and VitE can reduce oxidative stress by quenching/scavenging free radical intermediates, thereby preventing oxidative chain reactions.

Oxidative stress is considered a major player in neurodegenerative conditions such as Alzheimer’s (AD) and Parkinson’s (PD) diseases, and amyotrophic lateral sclerosis (ALS). ROS are produced during neuronal tissue injuries such as stroke and acute spinal cord injury (SCI).^{19–23} On the other hand, Q_{10} plays an essential role in the electron transport chain in mitochondria for ATP production. It can improve the general well-being of the aging population for their cardioprotective and hepatoprotective benefits.^{24,25} However, all these antioxidant compounds present major clinical translation challenges because of their poor water solubility and physicochemical stability in aqueous solutions and biological media. Additionally, their rapid metabolism leads to low bioavailability and restricted tissue distribution, affecting their efficacy.^{4,26,27} Particularly for Q_{10} , due to its high molecular weight (863 Da), light and temperature sensitivity, and high lipophilicity ($\log P = 21$ greater than that of CU and VitE), its applications as a therapeutic candidate have been limited.²⁵

We assume that encapsulating the antioxidants of interest into lipid liquid crystalline nanoparticles (LCNPs) can improve their solubility, stability, permeability, and dissolution profile, making them promising nanodrug candidates against oxidative stress and inflammation-mediated diseases. For this purpose, we selected monoolein (MO) and plasmalogen (PL) as lipid matrices to obtain fully sustainable and biocompatible nanoformulations of the bioactive compounds. Monoolein is extensively used as a cubic-phase-forming lipid in many applications. Plasmalogens belong to the vinyl ether-type glycerophospholipids and can significantly influence membrane organization, fluidity and dynamics. They may act as reservoirs for secondary messengers and precursors of inflammatory mediators within cell membranes.²⁸ To sterically stabilize the nanoformulations against aggregation, we chose three PEGylated amphiphiles: D- α -tocopherol polyethylene glycol-1000 succinate (TPGS-PEG₁₀₀₀), poly(ethylene glycol) monooleate derivative (MO-PEG₂₀₀₀), and N-(methylpolyoxyethylene oxycarbonyl)-1,2-distearoyl-*sn*-glycero-3-phosphoethanolamine, sodium salt (DSPE-PEG₂₀₀₀) along with the triblock copolymer Pluronic F127, comprising biocompatible poly(ethylene glycol) (PEG) and poly(propylene oxide) (PPO) units that may ensure long circulation of nanomedicines *in vivo*.²⁹

We aim to develop LCNP-based drug delivery systems of phytochemical nanotherapeutics by tuning the generated nanostructures and their physicochemical properties through an environmentally friendly green process employing the antioxidants CU, VitE, or Q_{10} . By using synchrotron small-angle X-ray scattering (SAXS) and quasi-elastic light scattering (QELS) we investigated the dynamic structural effects of the aqueous environment on nanoparticle topologies and sizes. We assessed the toxicity of the nanoparticles via MTT assays and evaluated their ability to scavenge free radicals for single or multiple loading of compounds with antioxidant properties.

MATERIALS AND METHODS

Materials. The PUFA-plasmalogen (vinyl ether) derivative 1-(1Zoctadecenyl)-2-docosahexaenoyl-*sn*-glycero-3-phosphoethanol-

amine (PL-DHA-PE) was obtained from Avanti Polar Lipids, Inc. (Alabama). According to the provider, the scallop-derived plasmalogen extract composition consists of ethanolamine vinyl ether phospholipid (49.4%), choline vinyl ether phospholipid (24.9%), cholesterol (16.0%), and ceramide aminoethyl phosphonate (9.7%). Monoolein (MO) (purity of >99%), Curcumin (CU) (purity of >66% in the curcuminoid mixture), coenzyme Q₁₀ (Q10), vitamin E (VitE), D- α -tocopherol polyethylene glycol-1000 succinate (TPGS-PEG₁₀₀₀), butylated hydroxytoluene (BHT), retinoic acid (RA), phosphate buffered saline, deficient of calcium and magnesium ions (PBS), fetal bovine serum (FBS), streptomycin-penicillin, trypsin, dimethyl sulfoxide (DMSO), and 3-(4,5-Dimethylthiazol-2-yl)-2,5-diphenyl tetrazolium bromide (MTT) were purchased from Sigma-Aldrich. The PEGylated lipids poly(ethylene glycol)monooleate NHS derivative (MO-PEG₂₀₀₀, Sunbrite OE-020CS) and N-(methylpolyoxyethylene oxycarbonyl)-1,2-distearoyl-*sn*-glycero-3-phosphoethanolamine, sodium salt (Sunbrite DSPE-PEG₂₀₀₀) were received from NOF Corporation (Tokyo, Japan). Water of Milli-Q quality (Millipore Corp., Molsheim, France) was used for the preparation of a phosphate buffer solution (NaH₂PO₄/Na₂HPO₄, 1×10^{-2} M, pH 7, p.a. grade, Merck).

Preparation of Nanoparticulate Liquid Crystalline Systems.

The liquid crystalline nanoparticles were prepared by the method of hydration of a lyophilized thin lipid film followed by physical agitation in an excess aqueous phase. The lipids monoolein and plasmalogen, the amphiphilic stabilizers TPGS-PEG₁₀₀₀, MO-PEG₂₀₀₀, DSPE-PEG₂₀₀₀ and Pluronic F127, and the antioxidants curcumin, vitamin E, and Q10 were weighed, dissolved in chloroform, and mixed at desired proportions (Table S2). The solvent was evaporated under a steady stream of nitrogen gas for 30 min at room temperature under a fume hood to create thin-film lipid samples. The samples were lyophilized overnight under cooling to remove the excess solvent. The thin-film samples were hydrated at room temperature in a solution of 1×10^{-2} M phosphate buffer (ph. b), stabilized with added butylated hydroxytoluene (BHT), prepared with Milli-Q water. The mixtures were fragmented and homogenized for 15 min using an ultrasonic ice bath at a frequency of 42 kHz. This process facilitates the self-assembly of different liquid crystalline nanostructures (cubosomes, hexosomes, and vesicles) at room temperature (22 °C).

Synchrotron Small-Angle X-ray Scattering (SAXS). SAXS measurements were carried out at the SWING beamline of the SOLEIL synchrotron (Saint Aubin, France). The wavevector, denoted as q , is given by $q = 4\pi \sin(\theta)/\lambda$, where 2θ represents the angle between the incident and scattered X-rays, and λ is the wavelength. The wavelength of the synchrotron radiation used was $\lambda = 1.033$ Å, with an exposure time of 500 ms. Calibration of the q -range was achieved using a silver behenate standard with a repeat spacing of $d = 58.38$ Å. The X-ray beam spot applied to the samples measured $375 \times 25 \mu\text{m}^2$. Data were captured using a two-dimensional Eiger X 4 M detector (Dectris, Baden-Daettwil, Switzerland) operating at 12 keV, covering a q -range from 0.0179 to 2.18 Å^{-1} . Samples were sealed in X-ray capillaries with a diameter of 1.5 mm and placed in a custom holder with (X, Y, Z) positioning.^{41,56} An average of five spectra was obtained per sample. The structural experiments were performed at 22 °C. The SAXS pattern of background samples consisting of (i) ph. b. with pH 7.0, and (ii) DMEM free of serum and phenol red with pH 7.4 were recorded for intensity background subtraction. Data analysis was performed using the ATSAS 3.2.1 software suite, specifically the PRIMUS module. Lattice parameters for the liquid crystalline lipid phases were determined by analyzing the Bragg peaks in the recorded diffraction patterns.

The periods of lamellar bilayer structures, denoted as d , were determined from the positions of the first-order diffraction peaks using the formula:

$$d = \frac{1}{S} \quad (1)$$

The lattice parameter of the inverted hexagonal phases, $a_{(\text{HII})}$, was calculated using the relationship:

$$a_{(\text{HII})} = d \left(\frac{2}{\sqrt{3}} \right) (h^2 + k^2 - hk)^{\frac{1}{2}} \quad (2)$$

where h and k are the Miller indices.

For cubic phases, the lattice parameter a_Q is calculated using the formula

$$a = d(h^2 + k^2 + l^2)^{\frac{1}{2}} \quad (3)$$

where the d -spacing is defined by Bragg's law,

$$d = \frac{2\pi}{q} \quad (4)$$

representing the repeat distance between scattering planes (i.e., $1/d^2 = (h^2 + k^2 + l^2)/a^2$).¹

Nanoparticles Size Determination. The size distributions of the liquid crystalline nanoparticles were measured with a Nano-ZS90 device from Malvern Instruments. The samples were dispersed in an aqueous phase and exposed to laser illumination, with scattered light intensity measured at a 90° angle by a photon detector. For stability studies, LCNPs were incubated with DMEM free of FBS and phenol red at a volume ratio of 1:1. The size distribution was analyzed at 1, 24, and 48 h. This process was conducted in triplicate at 25 °C. The refractive index and viscosity of Milli-Q water were 1.330 and 0.8872, respectively.

Cryogenic Transmission Electron Microscopy (cryo-TEM).

For cryo-TEM studies, a 2 μL sample droplet was placed on a lacey carbon film-covered copper grid (Science Services, Munich, Germany), hydrophilized by 30 s of glow discharge (Solarus, Gatan, Munich, Germany). Excess liquid was blotted to form a thin film over the lace holes. The sample was rapidly frozen in liquid ethane and cooled to 90 K using liquid nitrogen, maintaining constant temperature and humidity (Leica EMGP, Wetzlar, Germany). It was then transferred to a cryo-transfer holder (CT3500, Gatan, Munich, Germany) and examined with a Zeiss EM922 Omega energy-filtered TEM (EFTEM) instrument (Carl Zeiss Microscopy, Jena, Germany) at 200 kV. Zero-loss-filtered images ($DE = 0$ eV) were captured under reduced dose conditions ($100\text{--}1000 \text{ e/nm}^2$) with a bottom-mounted charge-coupled device (CCD) camera (Ultra Scan 1000, Gatan, Munich, Germany) processed with a digital imaging processing system (Digital Micrograph GMS 1.9, Gatan, Munich, Germany). Nanoparticle sizes matched the film thickness, with no deformations observed, and images were taken close to or slightly under focus to enhance contrast.¹²

DPPH Free Radical Scavenging Activity Assay. The free radical scavenging capacity of the LCNPs was assessed using the 2,2-diphenyl-1-picrylhydrazyl (DPPH) assay. Nanoparticles and Trolox, which served as a reference standard, were diluted to $1 \times 10^3 \mu\text{M}$. A stock DPPH solution (80 μM in ethanol) was prepared and stored in the dark at room temperature. For the assay, 50 μL of LCNP samples were mixed with 150 μL of DPPH solution in a 96-well plate and incubated in the dark for 5 min. The absorbance was measured at 517 nm using a microplate reader.⁵⁶ Antioxidant capacity was calculated as a percentage of DPPH radical scavenging capacity using a standard formula:

$$\text{inhibition (\%)} = \frac{A_0 - A_1}{A_0} \times 100 \quad (5)$$

where A_0 and A_1 are the absorbances of the control and test samples, respectively

Cell Viability Assay. SH-SY5Y Cells were seeded at a density of 20,000 cells/well seeded into 96-well plates and incubated overnight at 37 °C with 5% CO₂ to allow for adhesion. The medium was then replaced with a complete medium containing 10 μM retinoic acid (RA), and the cells were incubated for 5 days, with regular monitoring for differentiation. After 5 days, the RA-differentiated SH-SY5Y cells were deprived of fetal bovine serum (FBS) for 24 h and then treated with the desired formulations. Controls consisted of RA-differentiated SH-SY5Y cells also deprived of FBS for 24 h, referred to as RA/FBS(−). Post-treatment, the medium was removed, and 20 μL of MTT reagent (3-(4,5-dimethylthiazol-2-yl)-2,5-diphenyltetrazolium bromide) at a

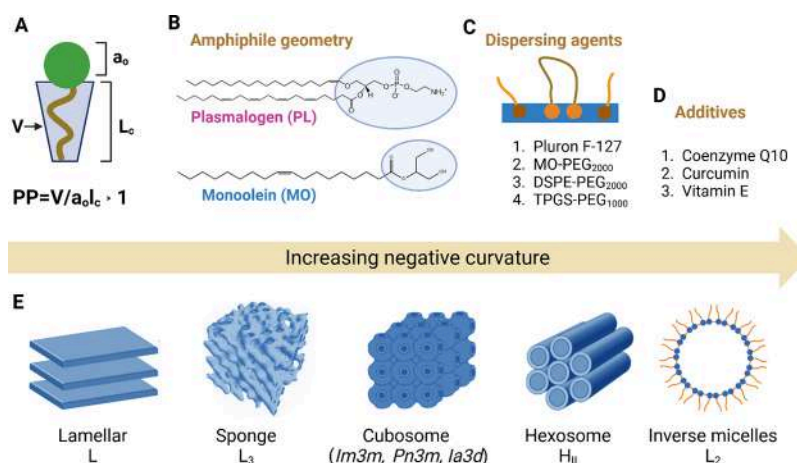


Figure 1. (A, B) Chemical structures of monoolein and plasmalogen with a representation of the molecular packing parameter (PP), where V is the hydrophobic chain volume, a_0 is the effective headgroup area, and l_c is the effective hydrophobic chain length. (C, D) Lists of dispersing agents and antioxidants used for creating LCNPs. (E) Lyotropic liquid crystalline phases of amphiphilic lipids in the order of increasing negative interfacial curvature. L: lamellar phase (zero curvature); L_3 : sponge phase; a schematic presentation of cubic phases, which may form cubosome nanoparticles of primitive cubic $Im3m$, diamond cubic $Pn3m$, or gyroid cubic $Ia3d$ space groups of symmetries; H_{II} : inverse hexagonal phase; and L_2 : inverse micellar aggregates.

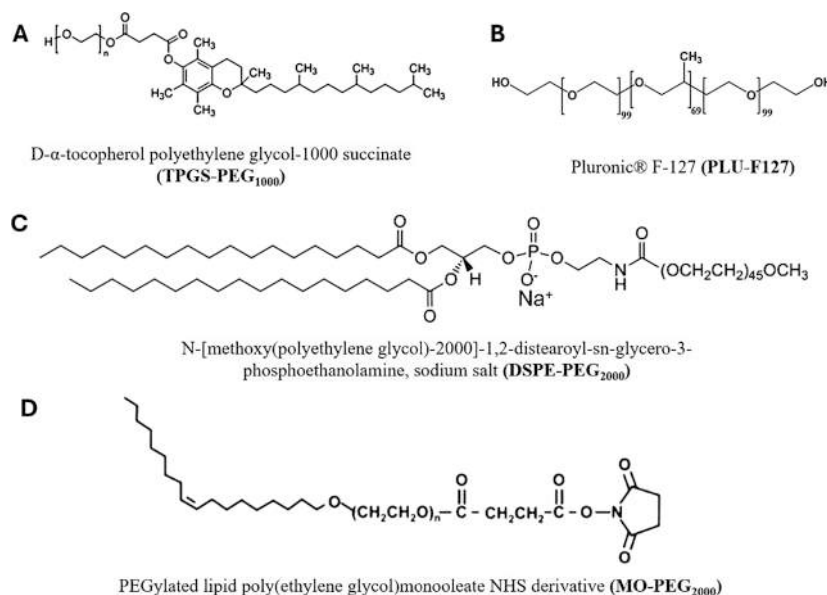


Figure 2. Chemical structures of the employed dispersing agents: (A) D- α -tocopherol polyethylene glycol-1000 succinate (TPGS-PEG₁₀₀₀), (B) Pluronic F127 (PLU-F127), (C) N-(methylpolyoxyethylene oxycarbonyl)-1,2-distearoyl-*sn*-glycero-3-phosphoethanolamine, sodium salt (DSPE-PEG₂₀₀₀), and (D) PEGylated lipid poly(ethylene glycol) monooleate NHS derivative (MO-PEG₂₀₀₀).

concentration of 5 mg/mL was added to each well and incubated for an additional hour. Subsequently, the medium was removed, and the formed formazan crystals were dissolved in DMSO. Cell viability was quantified by measuring absorbance spectrophotometrically at 570 nm (LT-5000 MS, Labtech). The MTT solution (5 mg/mL) was prepared in PBS and filtered before use.

Statistical Analysis. Statistical analysis was conducted using GraphPad prism version 8.0.1 analysis software. The data were presented as the mean \pm SD. Statistical significance was evaluated by one-way ANOVA or two-way ANOVA for multiple groups. p values of <0.05 were considered statistically significant.

RESULTS AND DISCUSSION

Structural Organization of Lipid-Based Liquid Crystalline Nanoassemblies for Loading of Multiple Antioxidants. *Self-Assembly of Single and Double-Chain Lyotropic Lipids as Host Membrane Nanocarriers.* For the

fabrication of nanoassemblies with tunable structures required for drug targeting, we exploited the structural polymorphism of different lipids with single (e.g., MO) or double chains (e.g., PL) to form nanoparticles embedding the antioxidant compounds of interest (curcumin, vitamin E, and coenzyme Q_{10}). The spontaneously organized nanosystem type is determined by the packing parameter (PP) and the intermolecular interactions with other molecules under the investigated environmental conditions (Figure 1).²⁸ Monoolein, a lipid (with $PP > 1$) known for forming nonlamellar liquid crystalline phases in many ternary systems,^{30,31} was combined with glycerophospholipids of the plasmalogen type to generate nanodispersions. Plasmalogens contain a vinyl ether bond at the *sn*-1 position and a polyunsaturated fatty acid chain at the *sn*-2 position (Figure 1B). When studied as lyotropic lipid systems, plasmalogens may self-assemble into various liquid crystalline mesophases, but their

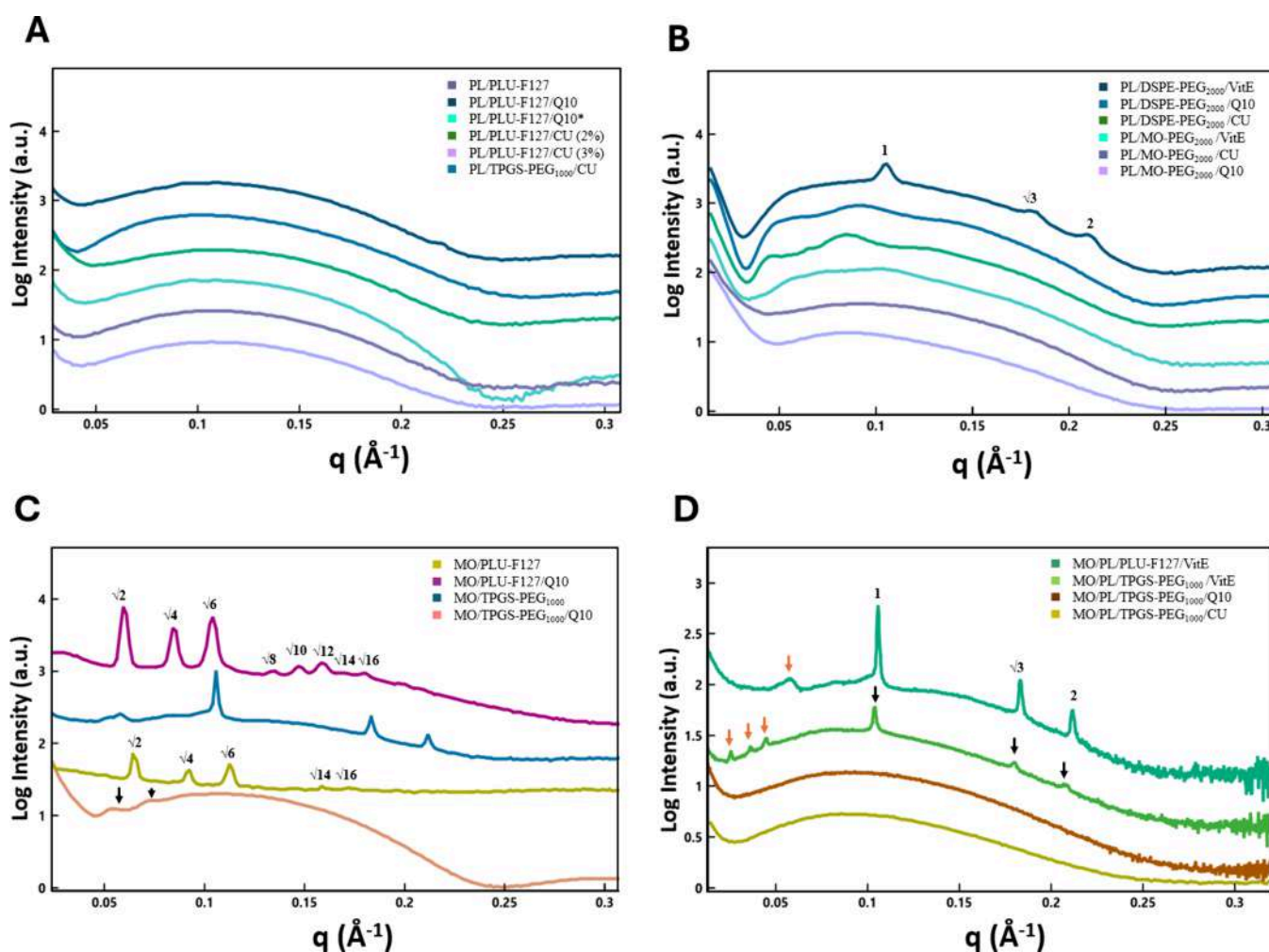


Figure 3. Representative synchrotron SAXS patterns of self-assembled lipid nanocarriers formed by MO, PL, or their mixtures. (A, B) SAXS patterns reveal the formation of PL-based vesicular or nonlamellar precursor phases at 22 °C. (C) SAXS patterns with well-defined Bragg peaks indexed with black arrows. The corresponding Miller indices are assigned to cubic $Im3m$ (purple and yellow plots) and inverted hexagonal H_{II} phase formation (blue plot) at 22 °C. (D) SAXS patterns of mixed MO/PL phospholipid nanocarriers indicating lamellar (bottom brown and yellow plots) and nonlamellar formations (deep green and light green plots).

specific phase behavior depends on factors such as hydrophobic chain length, degree of unsaturation, and the presence of other lipids or additives.²⁸

Choice of Dispersing Agents of Different Molecular Structures. To understand the impact of dispersing agents on nanoparticle formation, we employed Pluronic F127 (involving 100 PEG units) and three PEGylated amphiphiles: MO-PEG₂₀₀₀, DSPE-PEG₂₀₀₀, and TPGS-PEG₁₀₀₀ (Table S2). The goal was to assess the influence of structural polymorphism and the choice of dispersing agent on nanoparticle dispersion and stabilization at room temperature 22 °C (Figure 2).

Plasmalogen-Based Nanodispersions. The SAXS curves acquired for plasmalogen (PL)-based nanodispersions PL/PLU-F127 (Figure 3A) and PL/MO-PEG₂₀₀₀ (Figure 3B) are of a wide shape and indicate the formation of vesicular lipid particles. They were characterized by a broad hydrodynamic size distribution as determined by quasi-elastic light scattering (Table S1). Hexagonal-phase nano-objects form in the PL/DSPE-PEG₂₀₀₀/VitE system (Figure 3B, first plot from the top). Correspondingly, the observed Bragg diffraction peaks of a hexagonal phase in the SAXS pattern indicate that the nonlamellar phase is induced and predominates when the lipid

mixture includes VitE. Such a phase behavior can be attributed to the structural influence of the incorporated hydrophobic additive. The presence of small peaks in the SAXS patterns of the mixed nanossemblies stabilized by DSPE-PEG₂₀₀₀ (Figure 3B, second and third plot from the top) suggests the induction of intermediate states during the phase transition from bilayer vesicles to nonlamellar-type particles. Similar transitions have been reported for other mixed lipid systems as well.^{32–34}

Monoolein-Based Nanodispersions. The SAXS patterns acquired with MO-based lipid dispersions with (MO/PLU-F127/Q10) or without (MO/PLU-F127) small-molecule-antioxidant additives revealed distinct Bragg diffraction peaks (Figure 3C). The q -vector positions are spaced in the ratio $\sqrt{2} : \sqrt{4} : \sqrt{6} : \sqrt{8} : \sqrt{10} : \sqrt{12} : \sqrt{14} : \sqrt{16}$, and were indexed by the sequence of (110), (200), (211), (220), (310), (222), (321), and (400) reflections of a cubic lattice. They correspond to cubic phase structures of the $Im3m$ space group symmetry (Figure 3C, yellow and purple plots). The intensities of the (220), (310), and (222) peaks for the MO/PLU-F127 mixture were weaker as compared to those for the MO/PLU-F127/Q10 dispersions, reflecting a different electron density contrast upon inclusion of the Q10 compound. The cubic lattice parameter increased from

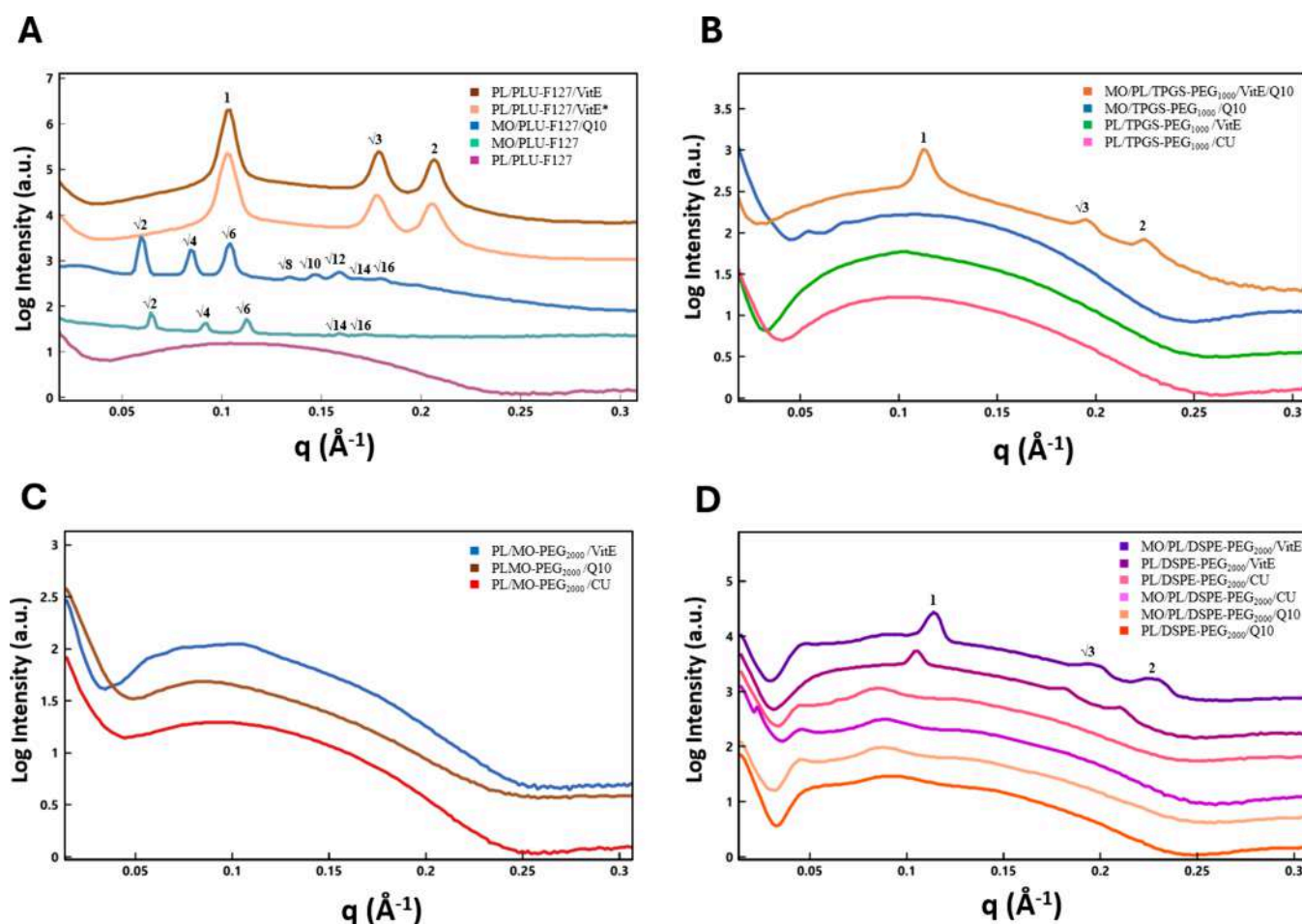


Figure 4. Synchrotron SAXS patterns of PL-based and MO-based lipid dispersions stabilized by (A) PLU-F127, (B) TPGS-PEG₁₀₀₀, (C) MO-PEG₂₀₀₀, and (D) DSPE-PEG₂₀₀₀ at temperature 22 °C. (A) SAXS profile displaying Bragg peaks of an inverted hexagonal H_{II} phase (first and second plots) and a cubic *Im3m* phase (third and fourth plots). The Bragg peaks of the nonlamellar phases are indexed by arrows. The black arrows in the first plot in panel (B) and the first and second plots in panel (D) indicate the presence of the H_{II} phase. The SAXS curves in (C) correspond to the formation of vesicular lipid membranes. The temperature is 22 °C.

$a_{Q(Im3m)} = 13.7$ to 14.8 nm in the presence of the Q10 additive (Table S3).

On the other hand, the structural investigation of the PEGylated MO/TPGS-PEG₁₀₀₀ and MO/TPGS-PEG₁₀₀₀/Q10 dispersions revealed a transition from hexagonal to lamellar phase structures that coexist with precursors of a cubic phase (Figure 3C, blue and pale orange plots). The observed significant structural difference between the MO/TPGS-PEG₁₀₀₀ and MO/TPGS-PEG₁₀₀₀/Q10 nanoassemblies can be attributed to the large size of the embedded hydrophobic Q10 molecules, which can influence the lipid bilayer and mesophase stability.^{35–40} It can be deduced that the incorporation of Q10 into the lipid phase may decrease the flexibility of the lipid/water interfaces, stabilize the lipid bilayer, and cause a structural change that favors the lamellar organization.

The mixed MO/PL lipid dispersions (MO/PL/TPGS-PEG₁₀₀₀/CU and MO/PL/TPGS-PEG₁₀₀₀/Q10) exhibited a lamellar (L) phase (Figure 3D, brown plot), while coexistence of H_{II} and *Im3m* cubic phases was observed, particularly for MO/PL/TPGS-PEG₁₀₀₀/VitE system (Figure 3D, light green plot). For MO/PL/PLU-F127/VitE, a shoulder peak indicated with an orange arrow appeared at $q = 0.058$ Å⁻¹, which may be attributed to the formation of precursors of a cubic phase in a coexistence with an H_{II} phase. Zhai et al. have identified a similar

correlation peak at $q = 0.05$ Å⁻¹ for Pluronic F127-stabilized phytantriol dispersions, attributing this phenomenon to the coexistence of an L_α phase and Q^D_{II} lattice structures.³⁸

Nanoparticulate Liquid Crystalline Structures Dispersed by the Block Copolymer Pluronic F127. The influence of Pluronic F127 on MO and PL nanodispersions was investigated across a range of F127 concentrations. The comparison aimed to understand the effects of the structural polymorphism and the use of Pluronic F127 or single- and double-chain PEGylated amphiphiles on nanoparticle dispersion and stabilization. The SAXS investigation of PLU-F127-stabilized dispersions of MO and PL revealed the induction of three distinct liquid crystalline phases depending on the composition (Figure 4). The nanostructures were identified by the resolved Bragg diffraction peaks, from which the lattice parameters of the different mesophases were determined (Table S4).

First, the SAXS patterns obtained at low Pluronic content (<10 wt %) in the MO/PLU-F127 mixture show the formation of a cubic phases of the *Im3m* space group (Figure 4A, third and fourth plots from the top). Bragg peaks were resolved with q -vector positions spaced in the ratio $\sqrt{2} : \sqrt{4} : \sqrt{6} : \sqrt{8} : \sqrt{10} : \sqrt{12} : \sqrt{14}$. They were assigned to the (110), (200), (211), (220), (310), (222) and (321) reflections of the primitive cubic phase of the *Im3m* space group. The diffraction peaks recorded

for the blank MO/PL-F127 nanocarriers were relatively weak compared to the Q10-containing lipid mixture MO/PLU-F127/Q10. The lattice parameters of the two cubic phase structures in the studied self-assembled systems were determined from the reciprocal slope of the linear plots, $q(\text{\AA}^{-1})$ versus $(h^2 + k^2 + l^2)^{1/2}$, where (hkl) are the Miller plane indices. The results are shown in Table S4.

Second, amphiphilic MO/PLU-F127 and PL/PLU-F127 mixtures were formulated at 12 and 17 wt % dispersing agent content (Figure 4A). The VitE-containing samples PL/PLU-F127/VitE and PL/PLU-F127/VitE* displayed three strong Bragg diffraction peaks in the SAXS patterns. These peaks are spaced in the ratio 1: $\sqrt{3}$:2 and are characteristic of a dominating inverted hexagonal (H_{II}) lattice that displays (10), (11), and (20) reflections. The Bragg peak maxima are positioned at $q_1 = 0.103 \text{ \AA}^{-1}$, $q_2 = 0.178 \text{ \AA}^{-1}$, and $q_3 = 0.205 \text{ \AA}^{-1}$. The H_{II} lattice parameter was determined by the relationship $a_{(HII)} = d(2/\sqrt{3})(h^2 + k^2 - hk)^{1/2}$, where h and k are the Miller indexes (Table S4).

Furthermore, the PL-based lipid mixture with a slightly increased Pluronic content (<20 wt %) (Figure 4A, bottom fifth plot) displayed a scattering profile of vesicular lipid membranes of a lipid bilayer organization derived from a lamellar liquid crystalline (L) phase. Bragg reflections corresponding to cubic or hexagonal phases were not detected for the dispersions of PL/PLU-F127, which may be attributed to a reduced interfacial curvature under the investigated conditions.

The lattice parameters, $a_{(Q)}$, of the cubic phase formed by the MO/PLU-F127 system with or without incorporated antioxidant molecules are presented in Table S4. The MO/PLU-F127/Q10 nanodispersion was characterized by a slightly higher cubic unit cell lattice parameter $a_{Q(Im3m)} = 14.8 \text{ nm}$ as compared to the blank nanocarrier MO/PLU-F127 ($a_{Q(Im3m)} = 13.7 \text{ nm}$). The lattice parameters of the inverted hexagonal (H_{II}) phases formed by the MO/PLU-F127/VitE and MO/PLU-F127/VitE* mixtures have values $a_{(HII)} = 7.0$ and 7.1 nm , respectively (Table S4).

Previous studies have indicated that Pluronic F127 (Poloxamer 407) can induce phase transitions toward a mesophase of lower negative curvature (Q_{II} , L_3 , and L_α phases).^{36–40} The poly(propylene oxide) [PPO] block of the polymer has an affinity for the polar to apolar interface of the lipid bilayer, resulting in an increased headgroup area (a_o) and formation of a phase with diminished negative curvature (i.e., lower PP).⁷ Although comparatively high Pluronic concentrations favor the formation of smaller nanoparticles (Table S1), they also promote the formation of vesicular systems. The mesophase shift from a lamellar to a nonlamellar cubic phase was observed at decreasing poloxamer concentrations. Therefore, the mixed self-assembled MO/PLU-F127 system requires a smaller quantity of a dispersing agent to undergo a structural transformation from a lamellar phase (vesicles) to cubic or inverted hexagonal mesophase structures (cubosomes/hexosomes).

Nanoparticulate Liquid Crystalline Structures Dispersed by PEGylated Amphiphiles. To investigate the influence of different PEGylated amphiphiles on the structural organization of the liquid crystalline nanosystems, synchrotron SAXS experiments were performed using different PEGylated lipids, namely, MO-PEG₂₀₀₀, DSPE-PEG₂₀₀₀, and TPGS-PEG₁₀₀₀ (Figure 3). The internal liquid crystalline structure of the nanoparticles dispersed by TPGS-PEG₁₀₀₀ exhibited three distinct Bragg peaks (Figure 4B, orange plot) with q -vector

positions indexed in the sequence 1: $\sqrt{3}$:2. They were assigned to the (10), (11) and (20) reflections of an inverted hexagonal (H_{II}) phase with a lattice parameter $a_{(HII)} = 6.5 \text{ nm}$ (Table S4). The SAXS plots of the other PEGylated nanosystems (MO/TPGS-PEG₁₀₀₀/Q10, MO/TPGS-PEG₁₀₀₀/VitE, and PL/TPGS-PEG₁₀₀₀/CU) displayed scattering curves characteristic of vesicular membranes derived from a predominating lamellar (L) phase (Figure 4B). Previous studies have indicated that L phases may appear at low water contents $\leq 30 \text{ wt } \%$.^{1,41} While a phase transition from L to inverse bicontinuous cubic phases ($1a3d$ and $Pn3m$ space groups) can occur at increased hydration levels above 30 wt %, we cannot attribute the observed phase behavior solely to the structure of the PEGylated blank lipid carrier (MO/PL/TPGS-PEG₁₀₀₀). Other factors, such as lipophilic additives (VitE and Q10), can influence the structural organization of the nanoparticle dispersions.

Similarly to the MO/PL/TPGS-PEG₁₀₀₀ stabilized nanoparticles, the amphiphilic mixture of PL/MO-PEG₂₀₀₀ also demonstrated a bilayer organization of the dispersed PL/MO-PEG₂₀₀₀ system (Figure 4C). The absence of sharp Bragg diffraction peaks indicated that the nanoparticles formed without a periodic multilamellar arrangement of lipid bilayers.

We further investigated by SAXS the self-assembled mixtures of MO and PL functionalized by the double-chain PEGylated phospholipid DSPE-PEG₂₀₀₀. The multicomponent MO/PL/DSPE-PEG₂₀₀₀/VitE and PL/DSPE-PEG₂₀₀₀/VitE mixtures adopted a hexosome-type organization (Figure 4D, first and second plot from top). The Bragg peak positions for the MO/PL/DSPE-PEG₂₀₀₀/VitE dispersion were resolved at $q_1 = 0.114 \text{ \AA}^{-1}$, $q_2 = 0.197 \text{ \AA}^{-1}$, and $q_3 = 0.228 \text{ \AA}^{-1}$ with a lattice parameter $a_{(HII)} = 6.4 \text{ nm}$. Comparatively, the scattering pattern for the PL/DSPE-PEG₂₀₀₀/VitE mixture showed a slightly lower intensity but similar Bragg peak positions, yielding a lattice parameter of $a_{(HII)} = 6.9 \text{ nm}$ for the inner structure of the hexosome-type LCNPs.

The four SAXS patterns in Figure 4D (plots 3–6 on the bottom) represent LCNP dispersions, revealing characteristic bumps at low q -vector values and indicating the absence of large domains of cubic mesophases. The positions of the broad maxima were observed at $q_1/q_2 = 0.045$, 0.085 \AA^{-1} and $q_1/q_2 = 0.054$, 0.092 \AA^{-1} for the PL/DSPE-PEG₂₀₀₀/CU and PL/DSPE-PEG₂₀₀₀/Q10 dispersions. For comparison, the position of the bump maxima for the MO/PL/DSPE-PEG₂₀₀₀ dispersion was observed at $q_1/q_2 = 0.046$ and 0.089 \AA^{-1} . The acquired SAXS pattern suggests a highly hydrated structure, where the inner periodic organization does not produce strong diffraction peaks (likely due to the small size of the nanoparticles and a limited number of repeat unit cell lattices, preventing significant Bragg diffraction).

The lack of a large-domain cubic phase structure in the SAXS pattern in Figure 4D (bottom panel) is consistent with a recent report demonstrating that PEGylated DOPG/DHA nanodispersions yield precursor structures. The latter were generated upon dispersion by TPGS-mPEG₂₀₀ and DSPE-mPEG₂₀₀₀ and exhibited similar weak broad correlation peaks, detected at $q = 0.40$ and 0.80 \AA^{-1} and $q = 0.50$ and 1.0 \AA^{-1} , respectively.³⁵ The DSPE-PEG₂₀₀₀ amphiphile influences the interfacial hydration state of the lipid bilayers⁴³ and can likely increase the fluidity of the MO/PL lipid membranes. Thus, the incorporation of DSPE-PEG₂₀₀₀ into MO/PL lipid bilayer interfaces can promote the formation of mesophases with reduced negative interfacial curvature due to the large hydrophilic PEG headgroup, which yields low PP (e.g., PP = 0.05).⁴²

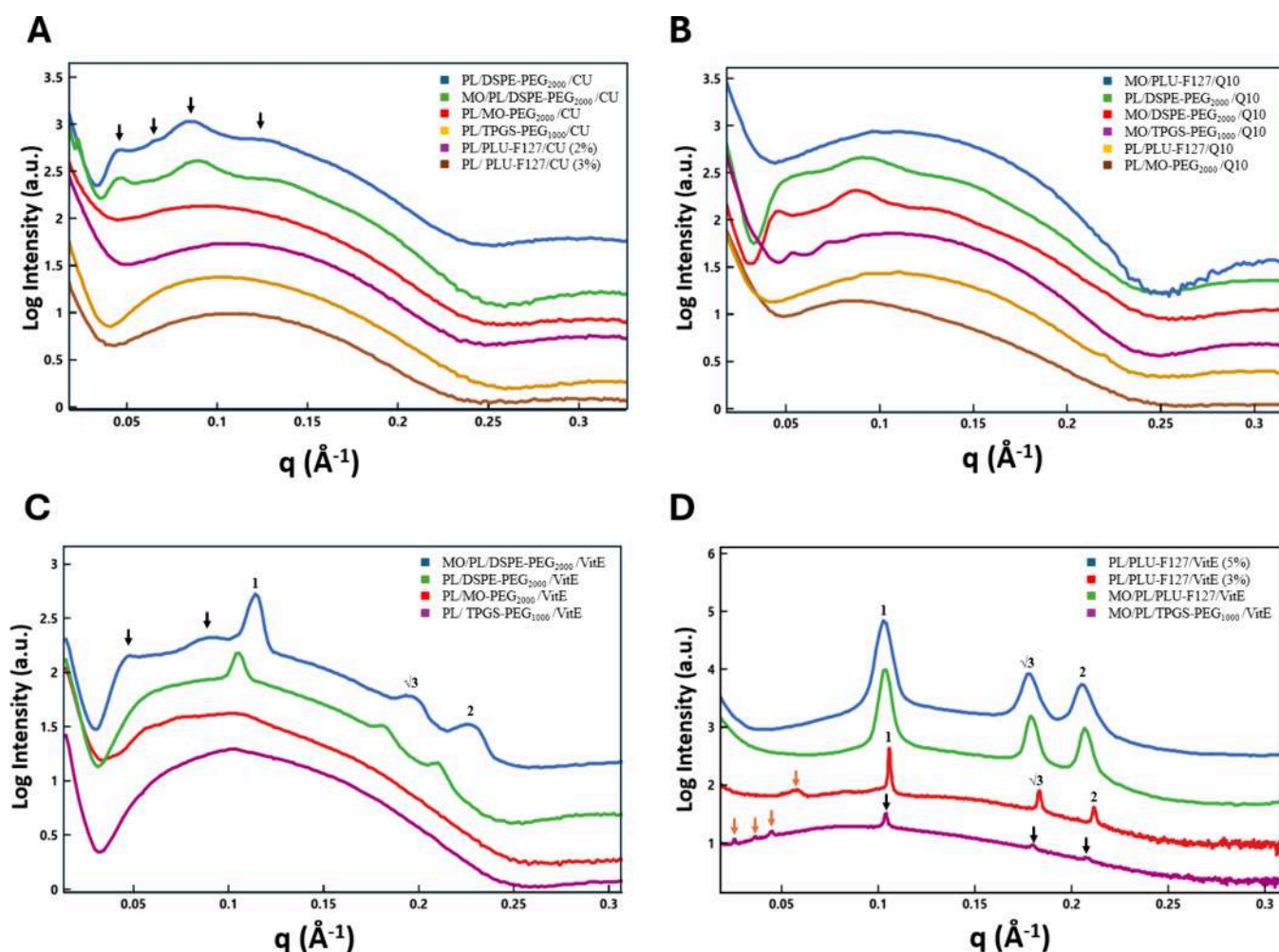


Figure 5. Small-angle X-ray scattering patterns showing the effect of adding hydrophobic small molecules to nanodispersions of monoolein and plasmalogen. (A–C) Lamellar structures dominate the organization of the self-assembled multicomponent mixtures involving CU, Q10, or VitE. (D) Nanodispersions of nonlamellar phases, for which the sets of Bragg peaks are indexed for an H_{II} and $Im3m$ (blue and green plots) phases, and mixed objects in an $H_{II}/Im3m$ cubic phase coexistence (purple plot on the bottom). The temperature is 22 °C.

Nanostructural Effect of Incorporated Hydrophobic Antioxidants in Self-Assembled Liquid Crystalline Structures.

The effect of incorporating three different hydrophobic small molecules in the studied liquid crystalline phases is presented in Figure 5. The antioxidant compound CU (see the SAXS data in Figure 5A) has a symmetrical structure with two hydrophobic aromatic rings connected by a flexible linker with hydrophilic hydroxyl groups. On the other hand, coenzyme Q10 has a long isoprenoid tail and a quinone headgroup that interact with the lipid bilayer, stabilizing vesicle formation (Figure 5B). The studied mixtures involving CU and Q10 favored lamellar bilayer phases except for the nanodispersions stabilized by DSPE-PEG₂₀₀₀. In the latter case, Figure 5A (blue and green plots) and Figure 5B (green and red plots) exhibited broad bumps in the SAXS patterns. They may represent a coexistence of vesicular membranes of different curvatures or the growth of intermediate architectures, starting from a nanovesicles that can dynamically fuse into developing 3D nanochannel network assemblies.^{33,34,44}

The obtained results indicated that VitE, which has a bulky hydrophobic moiety, favors the formation of nonlamellar phases, such as the inverted hexagonal (H_{II}) phase. This is agreement with other studies where the inclusion of hydrophobic drugs in lipid assemblies has induced a phase transition from the Q_{II} phase toward a more negatively curved H_{II} phase.⁷

Because the hydrophobic volume of VitE is bigger than that of CU, it is reasonable to expect that it may favor the formation of lipid structures with negative curvature. The structural effect of the employed surfactants on the VitE-loaded hexosomes was minimal (Figure 5). The lattice parameter for the PL/PL-F127 sample with 3 wt % VitE (at 9 wt % PL-F127) was $a_{(HII)} = 6.9$ nm (Figure 5D, red plot). It slightly increased to $a_{(HII)} = 7.1$ nm with increasing concentration of VitE in the mixture PL/Plu-F127/VitE (5 wt % VitE at 12 wt % PL-F127) (Figure 5D, blue plots). The acquired Bragg diffraction peaks were weaker for the hexosomes with lower VitE content.

The combination of MO and PL in the MO/PL/TPGS-PEG₁₀₀₀/VitE nanodispersion resulted in the coexistence of cubic $Im3m$ and hexagonal phases (Table S5). This finding reflects the miscibility of the main lipid components, from which the hydrated MO favors cubic mesophase formation, while plasmalogen can self-assemble into hexagonal or other structures.^{6,28,41}

Encapsulation of CU in liquid crystalline nanoparticles has been extensively reported in the literature. Regarding the biological activity of the LCNPs and their outcomes, a previous study has demonstrated that spongosome and cubosome nanoparticles coencapsulating curcumin (CU) and fish oil (FO) can significantly attenuate ROS accumulation in SH-SY5Y

cells.⁴⁵ Additionally, studies have shown that curcumin-DHA loaded carriers can modulate the BDNF/TrkB signaling pathway, which is essential for neuronal survival and repair in neurodegenerative disorders.⁴⁶ On the other hand, fewer studies have reported on the application of LCNPs containing Q₁₀ and VitE. Among these, recent work by Wu et al. has demonstrated that PUFA-plasmalogen-loaded LCNPs containing VitE and Q₁₀ can prolong CREB phosphorylation in a neurodegenerative disease model.⁴¹

Morphological Investigation by Cryo-TEM Imaging. Cryo-TEM imaging provided additional structural information to the SAXS analyses. The obtained cryo-TEM results (Figure 6)

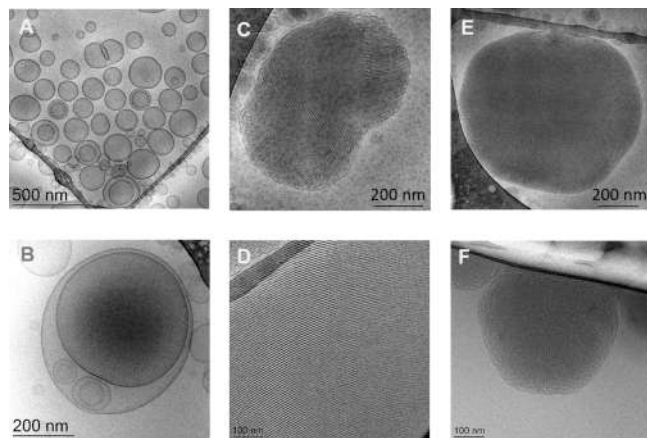


Figure 6. Cryo-TEM images of LCNPs demonstrating the topological diversity of the multicomponent structures established by SAXS. The dispersed liquid crystalline lipid mixtures generate nanoscale topologies of vesicular (A, B), hexosomal (C–F), or cubosomal (F) types.

confirmed that different dispersing agents and encapsulated hydrophobic bioactive compounds modulate the internal architecture of the LCNPs. This was achieved through the self-assembly of stable lamellar and nonlamellar liquid crystalline nanoparticles using amphiphilic lipids (MO and PL), single or double-chain PEGylated amphiphiles (MO-PEG₂₀₀₀, TPGS-PEG₁₀₀₀, and DSPE-PEG₂₀₀₀), as well as Pluronic F127. Multiphase nanostructures, which may arise locally in the core or periphery of the LCNPs, may be due to inhomogeneous membrane curvature distribution in the multicomponent assemblies.

Typical Cryo-TEM images of lipid membrane vesicles with different sizes are shown in Figure 6A,B. They correspond to amphiphilic mixtures with low interfacial membrane curvature, for instance those including the antioxidant compounds CU and Q₁₀ in the bilayers rich in double chain phospholipids.

Phase changes and lamellar bilayer-to-nonbilayer phase transitions were characteristic of the MO-based and the MO/PL-based nanoformulations. A nanoparticle with dense inner membrane organization and a lattice topology typical for cubosome lipid nanoparticles is presented in Figure 6F.

The mixed amphiphilic systems loaded with the small-molecule antioxidant VitE yielded self-assembled LCNPs of a predominantly hexosomal type. The examined sections of the nanoparticles, derived from an inverted-hexagonal (H_{II}) phase, displayed densely packed inner organization (Figure 6C–E). The H_{II}-phase structure consists of cylindrical water channels surrounded by lipid molecules arranged in a hexagonal lattice. Correspondingly, the cryo-TEM images show a series of parallel

lines, which correspond to the periodic arrangement of the lipid tubes in the densely packed hexagonal phase.

The observed distinct striations in Figure 6C,D are characteristic of the hexagonal arrangement of lipid/water interfaces within the studied hexosome nanoparticles. They represent a highly ordered internal structure of the lipid LCNPs. These striations are crucial for understanding the internal organization and stability of the hexosomes, which protect the encapsulated bioactive molecules in drug delivery applications.

Effect of Biological Cell Culture Medium on Nanoparticle Structural Stability and Size Distribution. The biodegradability and stability of LCNPs is a crucial aspect of green nanoparticle formulation. In a biological environment, LCNPs can change from a bimodal to a unimodal size distribution owing to structural transformations (Figure 7). To understand these biophysical characteristics, we incubated the antioxidant-loaded lipid nanoparticles in a cell culture medium (1:1 vol/vol ratio) prior to SAXS experiments. For this purpose, we selected the PL/PLU-F127/VitE, PL/PLU-F127/Q₁₀, MO/PLU-F127/Q₁₀, and MO/PL/TPGS-PEG₁₀₀₀/VitE/Q₁₀ dispersions for structural studies in Dulbecco's Modified Eagle Medium (DMEM) without fetal bovine serum (FBS) at pH 7.4. The resolved Bragg peaks were found to be weak for the PL/PLU-F127/VitE nanoparticles after 24 h postexposure to DMEM, particularly at $q_1 = 0.175 \text{ \AA}^{-1}$ and $q_2 = 0.201 \text{ \AA}^{-1}$ (Figure 7A). Overall, the exposure to DMEM did not destroy the integrity of the internal nanostructure. However, the lattice parameter was slightly higher upon DMEM incubation as compared to the intact nanoparticles stored in a phosphate buffer medium (Figure 7A–C). In contrast, a H_{II}-Lam phase transition was observed in the MO/PL/TPGS-PEG₁₀₀₀/VitE/Q₁₀ nanodispersion (Figure 7D). The structural behavior of hexosomal (H_{II}) systems has been studied by Bor et al. through incubation of DOPG/DHA nanodispersions in RPMI 1640 medium (containing 10% FBS) and Neurobasal-A medium.⁴⁷ The authors have determined time-dependent fluctuations in particle size distributions and emphasized that the sensitivity of the nanoparticles to the cell medium composition may be crucial for the nanoparticle-cell interaction kinetics.

After 24 h incubation of MO/PLU-F127/Q₁₀ nanoparticles in DMEM (Figure 7C), the Bragg peaks positions of the initial *Im3m* cubic phase were shifted to higher q -values. Accordingly, the exposure to DMEM resulted in a decrease in the cubic lattice parameter, $a_{(Q)}$, from 14.8 to 12.6 nm. The observed peak positions' shift was accompanied by the diminishment of the intensities of the (220), (310), (222), and (321) reflections of the *Im3m* cubic structure.

Recently, it has been demonstrated that cubosome-based nanostructures composed of monoolein and Pluronic F127/408 can be unstable in a biological environment as revealed by the observed rapid internal phase transition.^{48,49} Furthermore, Bode et al. have speculated that the internal nanostructure of the transformed dispersed particles was either an inverse hexagonal phase or an inverse micellar cubic (I₂) phase.⁴⁸ In contrast to these findings, our results indicate that the cubosomal nanoassemblies of the *Im3m* group remain stable in the cell culture medium and do not transform into a hexagonal phase. The replacement of MO with PL in the nanodispersion (PL/PLU-F127/Q₁₀) resulted in a structural shift from the H_{II} phase to a lamellar (L) phase (Figure 7B).

Next, we studied the effect of cell culture media (free of FBS and phenol red) on the hydrodynamic size distribution of PL/PLU-F127/VitE nanoparticles by DLS. The data in Table S1

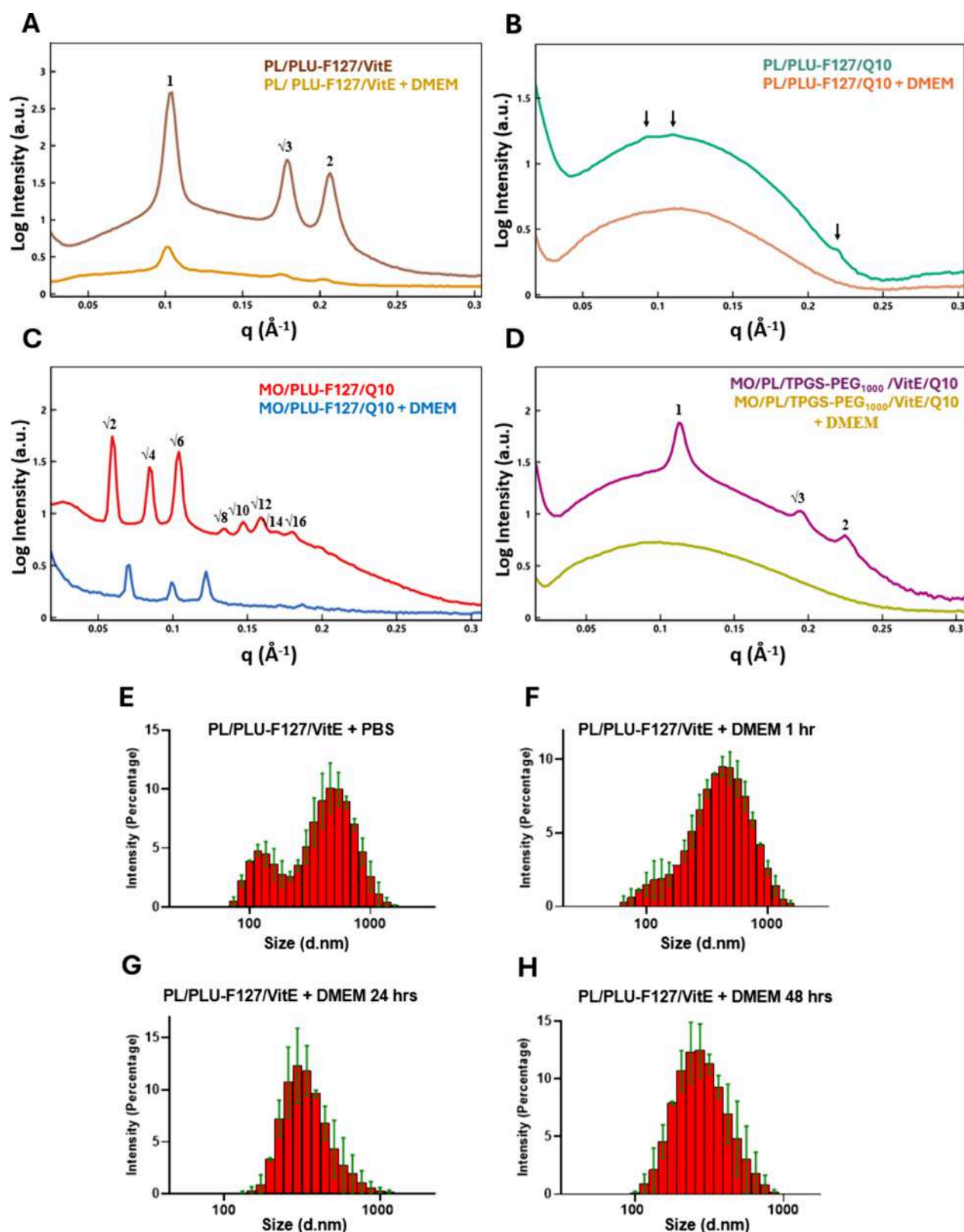


Figure 7. Small-angle X-ray scattering (SAXS) patterns of monoolein- or plasmalogen-based nanodispersions before and after 24 h incubation with the cell culture medium. (A) PL/PLU-F127/VitE, (B) PL/PLU-F127/Q10, (C) MO/PLU-F127/Q10, and (D) MO/PL/TPGS-PEG₁₀₀₀/VitE/Q10. (E–H) Hydrodynamic size distributions of PL/PLU-F127/VitE nanoparticles and their stability after 1, 24, and 48 h of incubation with a cell culture medium (DMEM) free of FBS and phenol red.

and Figure 7E–H show that the nanoparticle size distribution changes with the incubation time in DMEM. Following 1 h of incubation in the biological medium, the size distribution

dramatically changed from dual to single populations compared to the control nanoparticles in PBS (Figure 7E,F). The size continues to decrease after 24 and 48 h of incubation (Figure

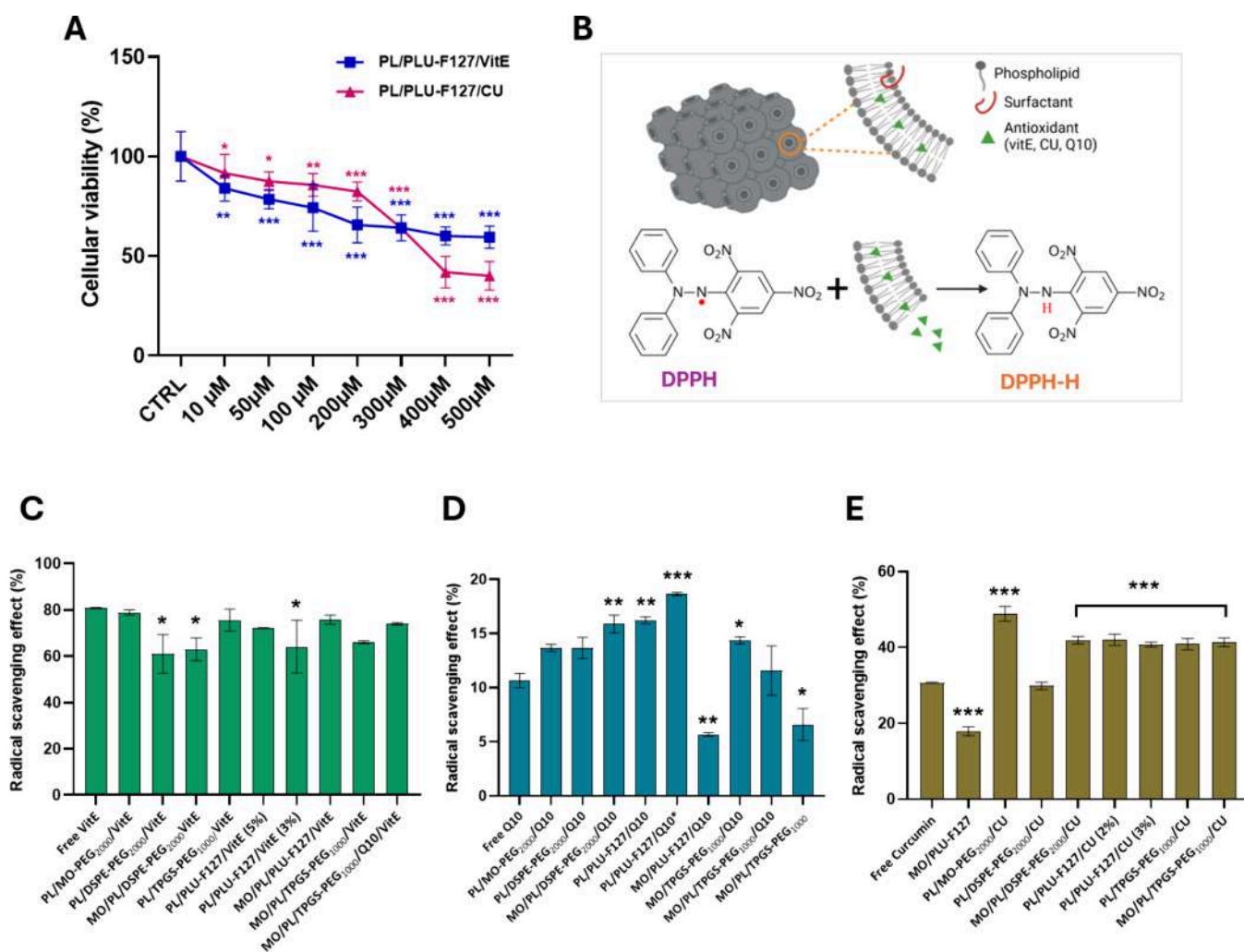


Figure 8. (A) Dose-dependent effect of PL/PLU-F127/VitE and PL/PLU-F127/CU nanoparticles on the viability of retinoic-acid (RA)-differentiated SH-SY5Y cells determined by MTT test. The cells were treated with increasing concentrations of LCNPs. The lipid concentration ranges were 10–500 μ M with reference to the total lipid concentration in the nanoparticle formulations. The cells differentiated by RA (10 μ M) for 7 days were considered a control group of 100% viability. Data are reported as mean \pm SD values relative to the control ($n = 6$, *** $p < 0.0005$, ** $p < 0.005$, * $p < 0.05$). Statistical differences were evaluated by two-way ANOVA. (B) Schematic mechanism of the radical scavenging ability of liquid crystalline nanoparticles loaded with antioxidant compounds. (C–E) Quantitative histograms of antioxidant activity of monoolein (MO)- or plasmalogen (PL)-based liquid crystalline nanocarriers of CU, Q10, and VitE, expressed as mean (%) of DPPH radical inhibition ($n = 2$). All p values are indicated with $p < 0.05$ considered as statistically significant. *** $p < 0.0005$, ** $p < 0.005$, and * $p < 0.05$ versus free CU, Q10, and VitE groups.

7G,H). This is in agreement with the SAXS data, which reflect a medium-dependent dynamic transformation from hexosomes to vesicles (Figure 7D). Considering that these dynamic alterations may influence nanoparticle interaction with cells, future work will be required to understand how these effects may affect the internalization mechanism of LCNPs.

In Vitro Antioxidant Activity of Liquid Crystalline Nanoparticles. After determining the viability of neuronally derived cells incubated with phytochemical-loaded LCNPs (Figure 8A and Figure S2), the scavenging effects of the LCNPs were compared with those of the free compounds (Figure 8). The activity of scavenging DPPH• radicals is based on single electron transfer (SET) or hydrogen atom transfer (HAT) reaction kinetics, reflecting the antioxidant capacity of substances (Figure 8B). The radical scavenging capacity of the CU, Q10, and VitE-loaded LCNPs was determined by DPPH radical scavenging assays, using free curcumin, Q10, and VitE as standard control groups. Figure 8C shows that encapsulated vitamin E and free VitE exhibit the highest radical scavenging

effects above 50% activity. They were found to be twice as potent as that of CU-loaded LCNPs measured by the DPPH assay (Figure 8E).

Among the three studied antioxidants, the scavenging effect of free CU suspension was 30.67%, which is relatively lower than that of the CU-loaded liquid crystalline nanocarriers (>40%), except for the blank MO/PLU-F127 nanocarriers and the PEGylated PL/DSPE-PEG₂₀₀₀/CU nanoparticles, which had the scavenging effects of 17.94% and 29.86%, respectively (Figure 8E). Studies have shown that free curcumin has very low solubility in water, leading to the formation of curcumin aggregates. The aggregation process reduces the amount of curcumin available to interact with free radicals, thereby diminishing its ability to donate hydrogen atoms to free radicals.⁵⁰ Encapsulation of curcumin within the studied nanoparticles (LCNPs) increases its bioavailability, thereby enhancing its antioxidant capacity.

Notably, both free CU and free Q10 showed lower scavenging effects compared to their encapsulated forms (Figure 8D,E).

This indicated that lipid crystalline nanoassemblies can significantly enhance the scavenging properties of antioxidants by providing a suitable microenvironment for the reaction with DPPH• radicals, facilitating the donation of hydrogen atoms to reduce DPPH• to nonradical forms. Additionally, the scavenging activity values of Q10 were below 30%, especially for MO/PLU-Q10 and MO/PL/TPGS-PEG₁₀₀₀, which exhibit the least antioxidant activity below 10%. Coenzyme Q10 (molecular weight 863 Da) presents characteristics including high lipophilicity (log P = 21) and poor water solubility (<4 ng/mL). These properties reduce its absorption efficiency and bioavailability, thus limiting its potential antioxidative and therapeutic applications both *in vitro* and *in vivo*. However, the increased antioxidant capacity of the plasmalogen (PL)-based nanoassemblies PL/PLU-F127/Q10 (Figure 8D) suggests that synergistic free radical scavenging effects can be achieved with the nanoformulations depending on their composition.

The mechanism of LCNPs for quenching free radicals depends on the ability of the nanomaterials to quench alkyl peroxy radicals by converting them to hydroperoxides. An interesting question is what is the mechanism of enhancement of antioxidant activity of lipid nanoparticles when they coencapsulate two antioxidants rather than a single compound? The enhancement of antioxidant activity in lipid nanoparticles when coencapsulating more than one phytochemical antioxidant can be attributed to several mechanisms: (i) when two antioxidants are coencapsulated, they can act together to neutralize free radicals more effectively than when used alone. This synergy may result from different mechanisms of action, where one antioxidant regenerates the other, or they target different types of free radicals; (ii) Phytochemical antioxidants may have complementary mechanisms of action. For example, one may be more effective at scavenging free radicals, while the other may influence the expression levels of oxidative enzymes (e.g., CAT, SOD, or GPx); (iii) Lipid nanoparticles can improve the bioavailability of the encapsulated antioxidants by facilitating their absorption and distribution *in vivo*. When two antioxidants are coencapsulated, they may be delivered more efficiently to the target sites. Moreover, lipid nanocarriers can dramatically change the pharmacokinetic properties of antioxidant drugs and control the release rates of the coencapsulated compounds. In perspective, it would be of interest to use release kinetic models to predict the release profile of antioxidant compounds and determine the key parameters that affect the release rate of coencapsulated phytochemicals. All these factors can contribute to the enhanced antioxidant activity observed with phytochemical coencapsulation, leading to more effective protection against oxidative stress and related damage.

***In Vitro* Toxicity of Liquid Crystalline Nanoassemblies of Vesicle, Hexosome, and Cubosome Types in Differentiated SH-SY5Y Cells.** The cytotoxicity of LCNPs constitutes an important property of drug delivery systems. In an *in vitro* environment, the toxicity of nanoparticles can be influenced by factors such as size, internal nanostructure, and chemical composition (lipids, dispersing agents, and included additives). The transition of the LCNPs from a lamellar to a cubic phase is hypothesized to enhance membrane fusion and facilitate transbilayer drug transport. Drug release is favored by nanoparticle dispersion from a large-size distribution into smaller-size populations.

In this study, PL/PLU-F127/CU and PL/PLU-F127/VitE nanoparticles were selected to investigate the dose–response effects of LCNPs on cellular viability of the human neuro-

blastoma cells (SH-SY5Y) as an *in vitro* model. Cells were exposed to varying concentrations (10–500 μ M) of the two nanoparticle formulations for 24 h. The results in Figure 8A demonstrate a dose-dependent decrease in cell viability. Notably, CU-loaded nanoparticles exhibited high toxicity at concentrations of 400 and 500 μ M, in contrast to the VitE-loaded nanoparticles. Although curcumin possesses a wide array of biological activities (including anti-inflammatory, antioxidant, and anticancer properties), its pro-oxidant activity can predominate at elevated concentrations, leading to cellular toxicity. Furthermore, curcumin can disrupt multiple signaling pathways, potentially resulting in cytotoxic effects.^{45,51–53}

Based on the dose–response experiments, we next studied the toxicity of MO/PL-based cubosomes, hexosomes, and vesicles stabilized by Pluronic F127 or PEGylation at a lipid concentration of 5 μ M. This concentration is suitable for comparison of the biological activities of the nanoparticles. Although the viability of cells treated with PL/MO-PEG₂₀₀₀/CU and MO/PL/DSPE-PEG₂₀₀₀/CU nanoformulations was significantly lower compared to the control, the viability remained above the critical threshold of 70%. The *in vitro* observed little toxicity of the MO- and PL-based LCNPs is in line with other studies that have analyzed the toxicity of MO-based cubosomes in the Hek293 and SH-SY5Y cell lines.^{45,54} Another study has explored the cytotoxicity of MO-based LCNPs and reported that 2D inverted hexagonal phase (H_{II}) nanoparticles were less toxic than the cubic-phase analogues.⁵⁵ Regarding the use of PEG as a stabilizer, Zhai et al. hypothesized that the elevated toxicity of PEGylated LCNPs can be attributed to the increased length of the PEG chains.⁴² The increased PEG chain length can create a denser surface on the nanoparticle, thereby enhancing the steric-entropic barrier, which can induce a cytotoxic effect. These studies suggest that the lyotropic lipid mesophase type and the effectiveness of the stabilizers are two important factors that may determine the *in vitro* cytotoxicity profiles. *In vivo*, toxicity and delivery studies will, therefore, be required to further optimize and assess the pertinency of these particles for therapeutic delivery applications.

CONCLUSIONS

We reported the nanostructural organization, stability, and enhanced ROS scavenging activity of multicomponent antioxidant-lipid assemblies of interest for developing phytochemical-based nanomedicines. To this aim, we employed a sustainable, simple-by-design approach for the cost-effective engineering of multiloading, self-assembled liquid crystalline nanoparticles. The combination of natural plant-based antioxidants, such as curcumin, coenzyme Q₁₀, and vitamin E, with nutraceuticals may enhance the effects of coadministered drugs, targeting various pathologies, including cancer, neurodegenerative disorders, cardiovascular, or infectious diseases. Lyotropic lipid liquid crystalline nanoparticles encapsulating phytochemical compounds can upregulate endogenous antioxidants (such as the enzymes CAT, SOD, GSH-Px, or proteins like Nrf2) and significantly reduce inflammatory cytokines (e.g., TNF- α and IL-6) and oxidative stress markers (e.g., MDA, 4-HNE, and 8-OHdG).

The structural variety among the designed phytochemical-loaded nanoassemblies, resulted in distinct liquid crystalline phases, including lamellar L, an inverted hexagonal H_{II}, and cubic *Im3m* phases. Our structural analysis revealed that antioxidants and dispersing agents can differently influence the structural polymorphisms of the lipid liquid crystalline phases of

MO and PL. Notably, vitamin E-loaded nanoparticles formed a nonlamellar H_{II} phase, while coenzyme Q₁₀ and curcumin favored a lamellar (L) phase. On the other hand, stabilizing the nanodispersions with Pluronic F127 yielded different mesophases (L, H_{II}, and cubic *Im3m*), whereas a PEGylated inverted hexagonal phase was observed when vitamin E was encapsulated into an initially lamellar nanostructure. Based on extensive structural characterization, we revealed the gradual dynamic alterations in nanoparticle-size distribution and structural features upon incubation in a biological cell culture medium. Taking into account the published evidence that the dynamic structural organization of the biodegradable nanoassemblies in the biological environment can affect the mechanism of nanoparticle interaction with cells (internalization and intracellular trafficking), future *in vitro* experiments would be necessary in this direction. Such experiments would help understand the uptake mechanisms of multiloaded liquid crystalline nanosystems with different architectural organizations that exert synergistic or quenching free radical scavenging effects. The proposed approach can open opportunities for the sustainable development of multifunctional lipid-based nanocarriers for site-specific targeting, inhibition of ROS-mediated inflammation, and more effective therapeutic interventions that could benefit from the controlled delivery of combinational phytochemical nanodrugs.

■ ASSOCIATED CONTENT

SI Supporting Information

The Supporting Information is available free of charge at <https://pubs.acs.org/doi/10.1021/acsbiomaterials.5c00006>.

Table S1: hydrodynamic diameters and polydispersity indices of lipid-based LCNPs; Table S2: compositions of monoolein and plasmalogen-based nanoformulations; Table S3: liquid crystalline structures and lattice parameters from synchrotron SAXS results (Figure 2); Table S4: SAXS-derived structure types and lattice parameters of PEGylated and PLU-F127-stabilized LCNPs (Figure 4); Table S5: vitamin E-loaded LCNPs structure types and parameters from SAXS results (Figure 5); Figure S1: SAXS fitting of PL/PLU-F127 nanocarriers using a spherical shell analytical model; Figure S2: cell viability of SH-SY5Y cells treated with LCNPs evaluated by MTT assay (PDF)

■ AUTHOR INFORMATION

Corresponding Author

Angelina Angelova — Université Paris-Saclay, CNRS, Institut Galien Paris-Saclay, Orsay 91400, France; orcid.org/0000-0002-0285-0637; Email: angelina.angelova@universite-paris-saclay.fr

Authors

Thelma Akanchise — Université Paris-Saclay, CNRS, Institut Galien Paris-Saclay, Orsay 91400, France

Borislav Angelov — Department of Structural Dynamics, Extreme Light Infrastructure ERIC, Dolni Brezany 252 41, Czech Republic; orcid.org/0000-0003-3131-4822

Yuru Deng — Wenzhou Institute, University of Chinese Academy of Sciences, Wenzhou 325001, China

Takehiko Fujino — Institute of Rheological Functions of Food, Fukuoka 811-2501, Japan

Thomas Bizien — Synchrotron SOLEIL, L'Orme des Merisiers, Saint-Aubin 91190, France; orcid.org/0000-0002-8779-7897

Complete contact information is available at:

<https://pubs.acs.org/doi/10.1021/acsbiomaterials.5c00006>

Author Contributions

The manuscript was prepared through the contributions of all authors. A.A. conceptualized and supervised the study; T.A., B.A., and A.A. contributed to the experimental investigation, data analysis, and data processing; B.A., Y.D., and T.F. provided materials and resources. T.B. contributed to instrument management and software; T.A. wrote the original draft; A.A. and B.A. reviewed and edited the manuscript. All authors critically reviewed the manuscript and approved the final manuscript for submission.

Notes

The authors declare no competing financial interest.

■ ACKNOWLEDGMENTS

T.A. acknowledges a PhD fellowship from Campus France. A.A. acknowledges membership in the CNRS GDR2088 BIOMIM research network. B.A. was funded by the project "Structural dynamics of biomolecular systems (ELIBIO)" (No. CZ.02.1.01/0.0/0.0/15_003/0000447) from the European Regional Development Fund, by the Czech Science Foundation (GACR project No. 24-10671S), and the Johannes Amos Comenius Operational Programme OPJAK (project No. SENDISO-CZ.02.01.01/00/22_008/0004596). The authors acknowledge the support provided by the SWING beamline of Synchrotron SOLEIL (Saint Aubin, France) and the allocation of beam time through projects 20210580 and 20230326. Figures ¹ and ⁸B were generated with BioRender.com.

■ ABBREVIATIONS

AD, Alzheimer's; ALS, amyotrophic lateral sclerosis; BDNF, brain-derived neurotrophic factor; CAT, catalase; CREB, cAMP response element-binding protein; PP, packing parameter; cryo-TEM, cryogenic transmission electron microscopy; CU, curcumin; DHA, docosahexaenoic acid; DLS, dynamic light scattering; DPPH, 2,2-diphenyl-1-picrylhydrazyl; DSPE-PEG₂₀₀₀, N-(methylpolyoxyethylene oxycarbonyl)-1,2-distearoyl-*sn*-glycero-3-phosphoethanolamine, sodium salt; FO, fish oil; GSH-Px, glutathione peroxidase; IL-6, interleukin 6; LCNPs, lyotropic liquid crystalline nanoparticles; MDA, malondialdehyde; MO, monoolein; MO-PEG₂₀₀₀, poly(ethylene glycol) monooleate NHS derivative; Nrf2, nuclear factor erythroid 2-related factor 2; PD, Parkinson's; PEG, poly(ethylene glycol); PL, plasmalogen; PLU-F127, Pluronic F127; PPO, poly(propylene oxide); PUFA, polyunsaturated fatty acid; Q10, coenzyme Q10; ROS, reactive oxygen species; SAXS, small-angle X-ray scattering; SCI, spinal cord injury; SOD, superoxide dismutase; TNF- α , Tumor Necrosis Factor alpha; TPGS-PEG₁₀₀₀, d- α -tocopherol polyethylene glycol-1000 succinate; TRKB, tropomyosin receptor kinase b; VitE, vitamin E; 4-HNE, 4-hydroxynonenal; 8-OHdG, 8-hydroxy-2'-deoxyguanosine

■ REFERENCES

(1) Rakotoarisoa, M.; Angelov, B.; Espinoza, S.; Khakurel, K.; Bizien, T.; Drechsler, M.; Angelova, A. Composition-Switchable Liquid Crystalline Nanostructures as Green Formulations of Curcumin and Fish Oil. *ACS Sustainable Chem. Eng.* **2021**, *9* (44), 14821–14835.

- (2) Hald Albertsen, C.; Kulkarni, J. A.; Witzigmann, D.; Lind, M.; Petersson, K.; Simonsen, J. B. The Role of Lipid Components in Lipid Nanoparticles for Vaccines and Gene Therapy. *Adv. Drug Delivery Rev.* **2022**, 188, No. 114416.
- (3) Varahachalam, S. P.; Lahooti, B.; Chamaneh, M.; Bagchi, S.; Chhibber, T.; Morris, K.; Bolanos, J. F.; Kim, N.-Y.; Kaushik, A. Nanomedicine for the SARS-CoV-2: State-of-the-Art and Future Prospects. *Int. J. Nanomed.* **2021**, 16, 539–560.
- (4) Ashok, A.; Andrabi, S. S.; Mansoor, S.; Kuang, Y.; Kwon, B. K.; Labhasetwar, V. Antioxidant Therapy in Oxidative Stress-Induced Neurodegenerative Diseases: Role of Nanoparticle-Based Drug Delivery Systems in Clinical Translation. *Antioxidants* **2022**, 11 (2), 408.
- (5) Abourehab, M. A. S.; Ansari, M. J.; Singh, A.; Hassan, A.; Abdelgawad, M. A.; Shrivastav, P.; Abualsoud, B. M.; Amaral, L. S.; Pramanik, S. Cubosomes as an Emerging Platform for Drug Delivery: A Review of the State of the Art. *J. Mater. Chem. B* **2022**, 10 (15), 2781–2819.
- (6) Barriga, H. M. G.; Holme, M. N.; Stevens, M. M. Cubosomes: The Next Generation of Smart Lipid Nanoparticles? *Angew. Chem. Int. Ed.* **2019**, 58 (10), 2958–2978.
- (7) Van 'T Hag, L.; Gras, S. L.; Conn, C. E.; Drummond, C. J. Lyotropic Liquid Crystal Engineering Moving beyond Binary Compositional Space – Ordered Nanostructured Amphiphile Self-Assembly Materials by Design. *Chem. Soc. Rev.* **2017**, 46 (10), 2705–2731.
- (8) Zhai, J.; Fong, C.; Tran, N.; Drummond, C. J. Nonlamellar Lyotropic Liquid Crystalline Lipid Nanoparticles for the Next Generation of Nanomedicine. *ACS Nano* **2019**, 13 (6), 6178–6206.
- (9) Clemente, I.; Lamponi, S.; Tamasi, G.; Rodolfi, L.; Rossi, C.; Ristori, S. Structuring and De-Structuring of Nanovectors from Algal Lipids: Simulated Digestion, Preliminary Antioxidant Capacity and In Vitro Tests. *Pharmaceutics* **2022**, 14 (9), 1847.
- (10) Yaghmur, A.; Mu, H. Recent Advances in Drug Delivery Applications of Cubosomes, Hexosomes, and Solid Lipid Nanoparticles. *Acta Pharmaceutica Sinica B* **2021**, 11 (4), 871–885.
- (11) Azmi, I. D. M.; Wibroe, P. P.; Wu, L.-P.; Kazem, A. I.; Amenitsch, H.; Moghimi, S. M.; Yaghmur, A. A Structurally Diverse Library of Safe-by-Design Citrem-Phospholipid Lamellar and Nonlamellar Liquid Crystalline Nano-Assemblies. *J. Controlled Release* **2016**, 239, 1–9.
- (12) Angelova, A.; Drechsler, M.; Garamus, V. M.; Angelov, B. Liquid Crystalline Nanostructures as PEGylated Reservoirs of Omega-3 Polyunsaturated Fatty Acids: Structural Insights toward Delivery Formulations against Neurodegenerative Disorders. *ACS Omega* **2018**, 3 (3), 3235–3247.
- (13) Vitoria Pupo Silvestrini, A.; Wender De Biasi, B.; Garcia Praça, F.; Vitoria Lopes Badra Bentley, M. Progress and Challenges of Lyotropic Liquid Crystalline Nanoparticles for Innovative Therapies. *Int. J. Pharm.* **2022**, 628, No. 122299.
- (14) Yaghmur, A.; Sartori, B.; Rappolt, M. Self-Assembled Nanostructures of Fully Hydrated Monoelaidin–Elaidic Acid and Monoelaidin–Oleic Acid Systems. *Langmuir* **2012**, 28 (26), 10105–10119.
- (15) Ganem-Quintanar, A.; Quintanar-Guerrero, D.; Buri, P. Monoolein: A Review of the Pharmaceutical Applications. *Drug Dev. Ind. Pharm.* **2000**, 26 (8), 809–820.
- (16) Clemente, I.; Falsini, S.; Di Cola, E.; Fadda, G. C.; Gonnelli, C.; Spinozzi, F.; Bacia-Verloop, M.; Grillo, I.; Ristori, S. Green Nanovectors for Phytodrug Delivery: In-Depth Structural and Morphological Characterization. *ACS Sustainable Chem. Eng.* **2019**, 7 (15), 12838–12846.
- (17) Marino, A.; Battaglini, M.; Moles, N.; Ciofani, G. Natural Antioxidant Compounds as Potential Pharmaceutical Tools against Neurodegenerative Diseases. *ACS Omega* **2022**, 7 (30), 25974–25990.
- (18) Martinelli, C.; Pucci, C.; Battaglini, M.; Marino, A.; Ciofani, G. Antioxidants and Nanotechnology: Promises and Limits of Potentially Disruptive Approaches in the Treatment of Central Nervous System Diseases. *Adv. Healthcare Materials* **2020**, 9 (3), No. 1901589.
- (19) Chen, X.; Ren, Q.; Chen, G.; Yi, Z.; Tong, Q.; Ran, Y.; Ma, L.; Fu, P.; Ma, L.; Li, X. Self-Assembled Phytochemical Nanomedicines with Enhanced Bioactivities for Effective Acute Kidney Injury Therapy. *ACS Sustainable Chem. Eng.* **2023**, 11 (19), 7288–7300.
- (20) Huang, X.; He, D.; Pan, Z.; Luo, G.; Deng, J. Reactive-Oxygen-Species-Scavenging Nanomaterials for Resolving Inflammation. *Materials Today Bio* **2021**, 11, No. 100124.
- (21) Zhang, C.; Wang, X.; Du, J.; Gu, Z.; Zhao, Y. Reactive Oxygen Species-Regulating Strategies Based on Nanomaterials for Disease Treatment. *Advanced Science* **2021**, 8 (3), No. 2002797.
- (22) Li, C.-W.; Li, L.-L.; Chen, S.; Zhang, J.-X.; Lu, W.-L. Antioxidant Nanotherapies for the Treatment of Inflammatory Diseases. *Front. Bioeng. Biotechnol.* **2020**, 8, 200.
- (23) Zhang, Y.; Chen, L.; Sun, R.; Lv, R.; Du, T.; Li, Y.; Zhang, X.; Sheng, R.; Qi, Y. Multienzymatic Antioxidant Activity of Manganese-Based Nanoparticles for Protection against Oxidative Cell Damage. *ACS Biomater. Sci. Eng.* **2022**, 8 (2), 638–648.
- (24) Pallotti, F.; Bergamini, C.; Lamperti, C.; Fato, R. The Roles of Coenzyme Q in Disease: Direct and Indirect Involvement in Cellular Functions. *IJMS* **2022**, 23 (1), 128.
- (25) Banun, V. J.; Rewatkar, P.; Chaudhary, Z.; Qu, Z.; Janjua, T.; Patil, A.; Wu, Y.; Ta, H. T.; Bansal, N.; Miles, J. A.; Ross, B. P.; Kumeria, T.; Popat, A. Protein Nanoparticles for Enhanced Oral Delivery of Coenzyme-Q10: In Vitro and in Silico Studies. *ACS Biomater. Sci. Eng.* **2023**, 9 (6), 2846–2856.
- (26) Akanchise, T.; Angelova, A. Potential of Nano-Antioxidants and Nanomedicine for Recovery from Neurological Disorders Linked to Long COVID Syndrome. *Antioxidants* **2023**, 12 (2), 393.
- (27) Cárdenas-Rodríguez, N.; Bandala, C.; Vanoye-Carlo, A.; Ignacio-Mejía, I.; Gómez-Manzo, S.; Hernández-Cruz, E. Y.; Pedraza-Chaverri, J.; Carmona-Aparicio, L.; Hernández-Ochoa, B. Use of Antioxidants for the Neuro-Therapeutic Management of COVID-19. *Antioxidants* **2021**, 10 (6), 971.
- (28) Angelova, A.; Angelov, B.; Drechsler, M.; Bizien, T.; Gorshkova, Y. E.; Deng, Y. Plasmalogen-Based Liquid Crystalline Multiphase Structures Involving Docosapentaenoyl Derivatives Inspired by Biological Cubic Membranes. *Front. Cell Dev. Biol.* **2021**, 9, No. 617984.
- (29) Chen, X.; Yi, Z.; Chen, G.; Ma, X.; Su, W.; Deng, Z.; Ma, L.; Tong, Q.; Ran, Y.; Li, X. Carrier-Enhanced Photodynamic Cancer Therapy of Self-Assembled Green Tea Polyphenol-Based Nanoformulations. *ACS Sustainable Chem. Eng.* **2020**, 8 (43), 16372–16384.
- (30) Kulkarni, C. V.; Wachter, W.; Iglesias-Salto, G.; Engelskirchen, S.; Ahualli, S. Monoolein: A Magic Lipid? *Phys. Chem. Chem. Phys.* **2011**, 13 (8), 3004–3021.
- (31) Qiu, H.; Caffrey, M. The Phase Diagram of the Monoolein/Water System: Metastability and Equilibrium Aspects. *Biomaterials* **2000**, 21 (3), 223–234.
- (32) Angelov, B.; Angelova, A.; Garamus, V. M.; Drechsler, M.; Willumeit, R.; Mutafchieva, R.; Štěpánek, P.; Lesieur, S. Earliest Stage of the Tetrahedral Nanochannel Formation in Cubosome Particles from Unilamellar Nanovesicles. *Langmuir* **2012**, 28 (48), 16647–16655.
- (33) Angelova, A.; Angelov, B.; Mutafchieva, R.; Lesieur, S. Biocompatible Mesoporous and Soft Nanoarchitectures. *J. Inorg. Organomet. Polym.* **2015**, 25 (2), 214–232.
- (34) Angelov, B.; Angelova, A.; Papahadjopoulos-Sternberg, B.; Lesieur, S.; Sadoc, J.-F.; Ollivon, M.; Couvreur, P. Detailed Structure of Diamond-Type Lipid Cubic Nanoparticles. *J. Am. Chem. Soc.* **2006**, 128 (17), 5813–5817.
- (35) Bor, G.; Lin, J.-H.; Lin, K.-Y.; Chen, H.-C.; Prajnamitra, R. P.; Salentini, S.; Hsieh, P. C. H.; Moghimi, S. M.; Yaghmur, A. PEGylation of Phosphatidylglycerol/Docosahexaenoic Acid Hexosomes with D- α -Tocopheryl Succinate Poly(Ethylene Glycol)₂₀₀₀ Induces Morphological Transformation into Vesicles with Prolonged Circulation Times. *ACS Appl. Mater. Interfaces* **2022**, 14 (43), 48449–48463.
- (36) Worle, G.; Drechsler, M.; Koch, M.; Siekmann, B.; Westesen, K.; Bunjes, H. Influence of Composition and Preparation Parameters on the Properties of Aqueous Monoolein Dispersions. *Int. J. Pharm.* **2007**, 329 (1–2), 150–157.

- (37) Johnsson, M.; Lam, Y.; Barauskas, J.; Tiberg, F. Aqueous Phase Behavior and Dispersed Nanoparticles of Diglycerol Monooleate/Glycerol Dioleate Mixtures. *Langmuir* **2005**, *21* (11), 5159–5165.
- (38) Zhai, J.; Fan, B.; Thang, S. H.; Drummond, C. J. Novel Amphiphilic Block Copolymers for the Formation of Stimuli-Responsive Nonlamellar Lipid Nanoparticles. *Molecules* **2021**, *26* (12), 3648.
- (39) Chountoules, M.; Perinelli, D. R.; Forys, A.; Chrysostomou, V.; Kaminari, A.; Bonacucina, G.; Trzebicka, B.; Pispas, S.; Demetzos, C. Development of Stimuli-Responsive Lyotropic Liquid Crystalline Nanoparticles Targeting Lysosomes: Physicochemical, Morphological and Drug Release Studies. *Int. J. Pharm.* **2023**, *630*, No. 122440.
- (40) Azhari, H.; Younus, M.; Hook, S. M.; Boyd, B. J.; Rizwan, S. B. Cubosomes Enhance Drug Permeability across the Blood–Brain Barrier in Zebrafish. *Int. J. Pharm.* **2021**, *600*, No. 120411.
- (41) Wu, Y.; Angelov, B.; Deng, Y.; Fujino, T.; Hossain, M. S.; Drechsler, M.; Angelova, A. Sustained CREB Phosphorylation by Lipid-Peptide Liquid Crystalline Nanoassemblies. *Commun. Chem.* **2023**, *6* (1), 241.
- (42) Zhai, J.; Hinton, T. M.; Waddington, L. J.; Fong, C.; Tran, N.; Mulet, X.; Drummond, C. J.; Muir, B. W. Lipid–PEG Conjugates Sterically Stabilize and Reduce the Toxicity of Phytantriol-Based Lyotropic Liquid Crystalline Nanoparticles. *Langmuir* **2015**, *31* (39), 10871–10880.
- (43) Hammel, M.; Fan, Y.; Sarode, A.; Byrnes, A. E.; Zang, N.; Kou, P.; Nagapudi, K.; Leung, D.; Hoogenraad, C. C.; Chen, T.; Yen, C.-W.; Hura, G. L. Correlating the Structure and Gene Silencing Activity of Oligonucleotide-Loaded Lipid Nanoparticles Using Small-Angle X-Ray Scattering. *ACS Nano* **2023**, *17* (12), 11454–11465.
- (44) Rizwan, S. B.; Dong, Y.-D.; Boyd, B. J.; Rades, T.; Hook, S. Characterisation of Bicontinuous Cubic Liquid Crystalline Systems of Phytantriol and Water Using Cryo Field Emission Scanning Electron Microscopy (Cryo FESEM). *Micron* **2007**, *38* (5), 478–485.
- (45) Rakotoarisoa, M.; Angelov, B.; Garamus, V. M.; Angelova, A. Curcumin- and Fish Oil-Loaded Spongosome and Cubosome Nanoparticles with Neuroprotective Potential against H₂O₂-Induced Oxidative Stress in Differentiated Human SH-SY5Y Cells. *ACS Omega* **2019**, *4* (2), 3061–3073.
- (46) Guerzoni, L. P. B.; Nicolas, V.; Angelova, A. In Vitro Modulation of TrkB Receptor Signaling upon Sequential Delivery of Curcumin-DHA Loaded Carriers Towards Promoting Neuronal Survival. *Pharm. Res.* **2017**, *34* (2), 492–505.
- (47) Bor, G.; Salentinig, S.; Şahin, E.; Nur Ödevci, B.; Roursgaard, M.; Liccardo, L.; Hamerlik, P.; Moghimi, S. M.; Yaghmur, A. Cell Medium-Dependent Dynamic Modulation of Size and Structural Transformations of Binary Phospholipid/ ω -3 Fatty Acid Liquid Crystalline Nano-Self-Assemblies: Implications in Interpretation of Cell Uptake Studies. *J. Colloid Interface Sci.* **2022**, *606*, 464–479.
- (48) Bode, J. C.; Kuntsche, J.; Funari, S. S.; Bunjes, H. Interaction of Dispersed Cubic Phases with Blood Components. *Int. J. Pharm.* **2013**, *448* (1), 87–95.
- (49) Leesajakul, W.; Nakano, M.; Taniguchi, A.; Handa, T. Interaction of Cubosomes with Plasma Components Resulting in the Destabilization of Cubosomes in Plasma. *Colloids Surf., B* **2004**, *34* (4), 253–258.
- (50) Yi, Z.; Cui, X.; Chen, G.; Chen, X.; Jiang, X.; Li, X. Biocompatible, Antioxidant Nanoparticles Prepared from Natural Renewable Tea Polyphenols and Human Hair Keratins for Cell Protection and Anti-Inflammation. *ACS Biomater. Sci. Eng.* **2021**, *7* (3), 1046–1057.
- (51) Bonaccorso, A.; Pellitteri, R.; Ruozi, B.; Puglia, C.; Santonocito, D.; Pignatello, R.; Musumeci, T. Curcumin Loaded Polymeric vs. Lipid Nanoparticles: Antioxidant Effect on Normal and Hypoxic Olfactory Ensheathing Cells. *Nanomaterials* **2021**, *11* (1), 159.
- (52) Anand, P.; Kunnumakkara, A. B.; Newman, R. A.; Aggarwal, B. B. Bioavailability of Curcumin: Problems and Promises. *Mol. Pharmaceutics* **2007**, *4* (6), 807–818.
- (53) McNally, S.; Harrison, E.; Ross, J.; Garden, O.; Wigmore, S. Curcumin Induces Heme Oxygenase 1 through Generation of Reactive Oxygen Species, P38 Activation and Phosphatase Inhibition. *Int. J. Mol. Med.* **2007**.
- (54) Hartnett, T. E.; Ladewig, K.; O'Connor, A. J.; Hartley, P. G.; McLean, K. M. Physicochemical and Cytotoxicity Analysis of Glycerol Monoolein-Based Nanoparticles. *RSC Adv.* **2015**, *5* (34), 26543–26549.
- (55) Tran, N.; Mulet, X.; Hawley, A. M.; Hinton, T. M.; Mudie, S. T.; Muir, B. W.; Giakoumatos, E. C.; Waddington, L. J.; Kirby, N. M.; Drummond, C. J. Nanostructure and Cytotoxicity of Self-Assembled Monoolein–Capric Acid Lyotropic Liquid Crystalline Nanoparticles. *RSC Adv.* **2015**, *5* (34), 26785–26795.
- (56) Akanchise, T.; Angelov, B.; Angelova, A. Nanomedicine-mediated Recovery of Antioxidant Glutathione Peroxidase Activity after Oxidative-stress Cellular Damage: Insights for Neurological Long COVID. *Journal of Medical Virology* **2024**, *96* (5), No. e29680.